

Analysis and reconstruction of the multiphase lattice Boltzmann flux solver for multiphase flows with large density ratios

Jinhua Lu 

Department of Mechanical Engineering, Chair of Aerodynamics and Fluid Mechanics, Technical University of Munich, Boltzmannstraße 15, Garching 85748, Germany and Department of Mechanics and Aerospace Engineering, Southern University of Science and Technology, Shenzhen 518055, China

Nikolaus A. Adams

Department of Mechanical Engineering, Chair of Aerodynamics and Fluid Mechanics, Technical University of Munich, Boltzmannstraße 15, Garching 85748, Germany and Munich Institute of Integrated Materials, Energy and Process Engineering, Technical University of Munich, Lichtenbergstr. 4a, Garching 85748, Germany

Peng Yu *

Department of Mechanics and Aerospace Engineering, Southern University of Science and Technology, Shenzhen 518055, China



(Received 15 February 2022; accepted 27 September 2022; published 17 October 2022)

The multiphase lattice Boltzmann flux solver (MLBFS) has been proposed to tackle complex geometries with nonuniform meshes. It also has been proven to have good numerical stability for multiphase flows with large density ratios. However, the reason for the good numerical stability of MLBFS at large density ratios has not been well established. The present paper reveals the relation between MLBFS and the macroscopic weakly compressible multiphase model by recovering the macroscopic equations of MLBFS (MEs-MLBFS) with actual numerical dissipation terms. By directly solving MEs-MLBFS, the reconstructed MLBFS (RMLBFS) that involves only macroscopic variables in the computational processes is proposed. The analysis of RMLBFS indicates that by combining the predictor step, the corrector step of MLBFS introduces some numerical dissipation terms which contribute to the good numerical stability of MLBFS. By retaining these numerical dissipation terms, RMLBFS can maintain the numerical stability of MLBFS even at large density ratios.

DOI: [10.1103/PhysRevE.106.045305](https://doi.org/10.1103/PhysRevE.106.045305)

I. INTRODUCTION

Based on the Boltzmann equation in statistical mechanics, the lattice Boltzmann method has been proven to be a simple and effective method in computational fluid dynamics. By discretizing the continuous distribution function, the lattice Boltzmann method [1] was first introduced in 1988 to simulate fluid flows. Since then, many lattice Boltzmann models for simulating multiphase flows have been formulated.

The first category is the color-gradient model proposed by Gunstensen *et al.* [2]. It introduces an additional two-phase collision step to reflect interfacial interactions caused by the surface tension and achieve phase separation. The second category is the pseudopotential multiphase lattice Boltzmann model proposed by Shan and Chen [3,4] to simulate single-component and multicomponent multiphase flows. It can achieve phase separation and thermodynamic consistency by introducing interparticle interaction forces. Recently, the model [5] with the self-tuning equation of state for multiphase flows was proposed as well. The third category

is the free energy model proposed by Swift *et al.* [6]. This model incorporates the nonideal equation of state into the pressure tensor of the Navier-Stokes equation to reflect the interfacial interaction. The fourth category is the interface tracking model proposed by He *et al.* [7]. It introduces another distribution function to capture the interface evolution by solving the phase-field equation.

The four kinds of multiphase lattice Boltzmann models track phase interfaces with different approaches. However, these original models are unstable for multiphase flows with large density ratios (like water-air flow with a density ratio of about 1000) [8]. Therefore, some improved models were proposed to deal with the problem, and some typical improved models are introduced as follows.

In the category of color-gradient models, based on a modified recoloring operator, Leclaire *et al.* [9] proposed an isotropic color gradient model that can handle very high-density ratios for a stationary bubble immersed in another fluid by using an isotropic gradient discretization. By adding a source term to exactly recover the Navier-Stokes equations, Ba *et al.* [10] proposed a multiple-relaxation-time color-gradient lattice Boltzmann model for simulating two-phase flows with large density ratios. In the category of

*yup6@sustech.edu.cn

pseudopotential models, Li *et al.* [11] proposed an improved forcing scheme for the multiple-relaxation-time pseudopotential lattice Boltzmann model to achieve thermodynamic consistency, and a large density ratio can be achieved with the model as a result. In the category of free energy models, Zheng *et al.* [12] proposed a Galilean-invariant free energy model that can be used to model multiphase flows with large density ratios beyond 1000. In the category of interface tracking models, Lee and Lin [13] proposed a stable discretization scheme based on the idea of directional derivatives. Fakhari *et al.* [14] proposed an improved model that does not need to use biased or mixed difference stencils.

However, all these models mentioned above are based on the unit lattice framework and therefore share some intrinsic drawbacks. The first and the most significant one is the limitation of a uniform mesh, which makes the treatment of complex geometry complicated [15,16]. The second one is that the time step is coupled with the mesh size, which makes the implementations of the adaptive and multiblock computations complicated [17,18]. The third one is the extra memory size to store distribution functions. For example, a D3Q19 model needs to store extra 19 distribution functions for each computational node.

To overcome the three drawbacks and achieve good numerical stability at high-density ratios, Wang *et al.* [19] proposed a multiphase lattice Boltzmann flux solver (MLBFS) for incompressible multiphase flows with large density ratios. It is a finite volume solver that reconstructs a simplified lattice Boltzmann model at the mesh interface to calculate pressure and momentum fluxes. The phase interface is captured by directly solving the macroscopic Cahn-Hilliard equation. Consequently, the three intrinsic drawbacks of the multiphase lattice Boltzmann models can be overcome. Simultaneously, MLBFS shows good numerical stability for multiphase flows with high-density ratios. Based on the same idea, Shi *et al.* [20] extended the original MLBFS for binary fluid flows to three-component fluid flows.

In the original MLBFS, the computation of the compensation tensor introduces additional complexity and usually needs a relatively thicker interface thickness to maintain numerical stability, which makes the solver complex and inefficient. By modifying the computation of the interface fluxes, the improved MLBFS [21] was proposed. It not only avoids the calculation of the compensation tensor but also can maintain numerical stability with very thin interface thickness.

In the two MLBFS models proposed by Wang *et al.* [19,21], the phase interface is tracked by directly solving the Cahn-Hilliard equation. To achieve good numerical stability and accuracy, the fifth-order Weighted Essentially Non-Oscillatory scheme (WENO) scheme [22] is applied to discretize the convection term in the Cahn-Hilliard equation. However, the WENO scheme has a rigorous requirement for the mesh, which spoils the ability of MLBFS models to tackle complex geometries by using nonuniform meshes. To achieve flexibility for complex geometry, Li *et al.* [23] proposed an interfacial lattice Boltzmann flux solver (ILBFS) to solve the Cahn-Hilliard equation, which allows all governing equations to be solved within the lattice Boltzmann flux solver framework. Based on ILBFS, Yang *et al.* [24,25] proposed the simplified MLBFS with lower computational cost [24]

and an improved MLBFS with better numerical stability and accuracy [25].

Although these MLBFS models have been successfully applied to simulate multiphase flows with large density ratios, the reason for the good numerical stability at large density ratios has not been well explained. On the one hand, the procedures to calculate interface fluxes in these models involve only macroscopic variables, which indicates that these models are macroscopic models intrinsically. On the other hand, the recovered governing equations of MLBFS models indicate that they simulate incompressible multiphase flows with the weakly compressible model. However, it has been proven that for both macroscopic weakly compressible models for single-phase flows and multiphase flows, additional treatments [26,27] are needed, in general, to improve the numerical stability. Therefore, the present paper aims to show the relation between MLBFS and the macroscopic weakly compressible multiphase model and then reveal the reason for the good numerical stability of MLBFS.

In the present paper, macroscopic equations of MLBFS (MEs-MLBFS) are derived first by approximating its actual computational process. Unlike the recovered macroscopic equations, which aim to recover the standard governing equations, given by Wang *et al.* [19], the present MEs-MLBFS retain the discretized macroscopic equations of the predictor step to analyze the actual numerical dissipation terms. By solving MEs-MLBFS with a finite volume scheme, the reconstructed MLBFS (RMLBFS) is proposed. The reason for the good numerical stability of MLBFS at large density ratios is analyzed by investigating the numerical dissipation terms in MEs-MLBFS.

The remainder of this paper is organized as follows. Section II introduces MLBFS. Section III derives MEs-MLBFS and proposes RMLBFS. Section IV analyzes the reason for the good numerical stability of MLBFS. In Sec. V, six benchmark tests are simulated to validate RMLBFS. Finally, conclusions are given in VI.

II. MULTIPHASE LATTICE BOLTZMANN FLUX SOLVERS

A. Governing equations of incompressible multiphase flow

The macroscopic governing equations for simulations of incompressible multiphase flows recovered by the lattice Boltzmann model [13] are

$$\partial_t p + \rho c_s^2 \partial_\alpha u_\alpha = 0, \quad (1)$$

$$\partial_t(\rho u_\alpha) + \partial_\beta(\rho u_\alpha u_\beta) = -\partial_\alpha p + \partial_\beta(\mu \partial_\alpha u_\beta + \mu \partial_\beta u_\alpha) + F_\alpha, \quad (2)$$

where ρ is the fluid density, u_α is the velocity, p is the pressure, F_α is the forcing term, and subscripts α and β are the coordinate components. The Cahn-Hilliard equation is applied to capture the phase interface, which can be given as

$$\partial_t C + \partial_\alpha(u_\alpha C) = M_C \nabla^2 \mu_C, \quad (3)$$

where C is the volume fraction of the heavier fluids, M_C is the constant mobility, and μ_C is the chemical potential determined by the total free energy of fluid-fluid or fluid-wall interfaces. The local density ρ and kinematic viscosity ν are determined

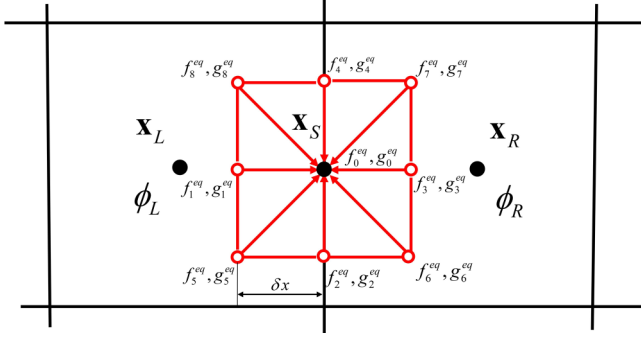


FIG. 1. The reconstructed lattice Boltzmann model at the interface.

by the heavier (subscript H) and lighter (subscript L) fluids:

$$\rho = \rho_H C + (1 - C)\rho_L, \quad 1/\nu = C/\nu_H + (1 - C)/\nu_L. \quad (4)$$

The total free energy is given as

$$F_E(C, \nabla C) = \int_V \left[E_0(C) + \frac{\kappa}{2} |\nabla C|^2 \right] dV + \int_S \varphi(C_S) dS, \quad (5)$$

where $E_0(C)$ is the bulk free energy defined as $E_0(C) = \lambda C^2(C - 1)^2$, λ and κ are fixed parameters, and $\varphi(C_S)$ is the wall free energy per unit area. For the equilibrium state, the total free energy is minimized, and therefore the chemical potential μ_C of the inside fluid can be determined by

$$\mu_C = -\frac{\partial E_0}{\partial C} - \kappa \nabla^2 C = 2\lambda C(C - 1)(2C - 1) - \kappa \nabla^2 C. \quad (6)$$

Once the thickness of the interface ξ and the interfacial tension force σ are given, parameters λ and κ can be determined by

$$\sigma = \sqrt{2\kappa\lambda}/6, \quad \kappa = \lambda\xi^2/8. \quad (7)$$

The expression of the surface tension force can be written as

$$F_{S\alpha} = -C\partial_\alpha\mu_C. \quad (8)$$

For a solid-fluid boundary, first, to ensure the mass conservation law, the boundary condition for μ_C at the wall is given as

$$n_\alpha \partial_\alpha \mu_C|_{\text{wall}} = 0, \quad (9)$$

where n_α is the unit outer normal vector. Second, to minimize the total free energy contributed by the specified wall free energy, the boundary condition for C can be given as

$$n_\alpha \partial_\alpha C|_{\text{wall}} = \epsilon (C_{\text{wall}} - C_{\text{wall}}^2) \sqrt{2\lambda/\kappa}, \quad (10)$$

where ϵ is related to the equilibrium contact angle θ^{eq} at the three-phase contact line through

$$\cos \theta^{eq} = -\epsilon. \quad (11)$$

B. MLBFS

In the original MLBFS [21], the phase-field equation is not solved in the framework of the lattice Boltzmann flux solver. Later ILBFS [23] for the phase-field equation was proposed. In the present paper, to unify the computational scheme, the MLBFS used for analysis is a combination of MLBFS [21] for pressure and Navier-Stokes equations and ILBFS [23] for the phase-field equation. The discretized governing equations of MLBFS are

$$\frac{\partial p}{\partial t} + \frac{1}{\Delta V} \sum_k R_\alpha \Delta S_k n_{k\alpha} = u_\alpha \partial_\alpha (\rho c_s^2), \quad (12)$$

$$\frac{\partial (\rho u_\alpha c_s^2)}{\partial t} + \frac{1}{\Delta V} \sum_k \Pi_{\alpha\beta} \Delta S_k n_{k\alpha} = F_\alpha c_s^2, \quad (13)$$

$$\frac{\partial C}{\partial t} + \frac{1}{\Delta V} \sum_k Q_\alpha \Delta S_k n_{k\alpha} = 0, \quad (14)$$

where R_α , $\Pi_{\alpha\beta}$, and Q_α are interface fluxes, c_s is the sound speed, ΔV is the control volume, subscript k denotes the k th interface of the control volume, ΔS_k is the area of the k th interface, and $n_{k\alpha}$ is the outer normal vector of the k th interface. The detailed procedures to calculate interface fluxes through reconstructing a local lattice Boltzmann model are introduced as follows.

(a) Reconstruction of the local lattice Boltzmann model: As shown in Fig. 1, a unit lattice of the D2Q9 model is constructed at the interface center. The discrete velocities of the D2Q9 model are

$$\begin{aligned} \text{D2Q9} : \mathbf{e}_i \\ = \begin{bmatrix} 0 & 1 & 0 & -1 & 0 & 1 & -1 & -1 & 1 \\ 0 & 0 & 1 & 0 & -1 & 1 & 1 & -1 & -1 \end{bmatrix} c. \end{aligned} \quad (15)$$

As to 3D cases, the D3Q19 model is adopted and the discrete velocities are

$$\text{D3Q19} : \mathbf{e}_i = \begin{bmatrix} 0 & 1 & -1 & 0 & 0 & 0 & 0 & 1 & -1 & 1 & -1 & 1 & -1 & 0 & 0 & 0 & 0 & 0 \\ 0 & 0 & 0 & 1 & -1 & 0 & 0 & 1 & 1 & -1 & -1 & 0 & 0 & 0 & 1 & -1 & 1 & -1 \\ 0 & 0 & 0 & 0 & 0 & 1 & -1 & 0 & 0 & 0 & 0 & 1 & 1 & -1 & 1 & 1 & 1 & -1 & -1 \end{bmatrix} c. \quad (16)$$

(b) Calculation of the distribution functions at $(\mathbf{x}_S - \mathbf{e}_i \delta t, t)$: The interpolation scheme to calculate p , u_α and C at $\mathbf{x}_S - \mathbf{e}_i \delta t$ is

$$\phi = \begin{cases} \phi_L + \nabla \phi_L \cdot (\mathbf{x}_S - \mathbf{e}_i \delta t - \mathbf{x}_L) & \mathbf{x}_S - \mathbf{e}_i \delta t \text{ at the left cell} \\ \phi_R + \nabla \phi_R \cdot (\mathbf{x}_S - \mathbf{e}_i \delta t - \mathbf{x}_R) & \mathbf{x}_S - \mathbf{e}_i \delta t \text{ at the right cell} \\ 0.5[\phi_L + \nabla \phi_L \cdot (\mathbf{x}_S - \mathbf{e}_i \delta t - \mathbf{x}_L)] \\ + 0.5[\phi_R + \nabla \phi_R \cdot (\mathbf{x}_S - \mathbf{e}_i \delta t - \mathbf{x}_R)] & \mathbf{x}_S - \mathbf{e}_i \delta t \text{ at the interface,} \end{cases} \quad (17)$$

where ϕ denotes an arbitrary variable, and the subscripts S , L , and R denote the variables at the interface, left cell, and right cell, respectively. The partial derivatives at cell centers are calculated by the discretized Gauss theorem

$$\Delta V \partial_\alpha \phi = \sum_k \phi_S \Delta S_k n_{k\alpha}. \quad (18)$$

The macroscopic variables at the interface in Eq. (18) are obtained by a linearized interpolation

$$\begin{aligned} \phi_S &= \frac{\phi_L |\mathbf{x}_R - \mathbf{x}_S|}{|\mathbf{x}_R - \mathbf{x}_S| + |\mathbf{x}_L - \mathbf{x}_S|} \\ &+ \phi_R \left(1 - \frac{|\mathbf{x}_R - \mathbf{x}_S|}{|\mathbf{x}_R - \mathbf{x}_S| + |\mathbf{x}_L - \mathbf{x}_S|} \right). \end{aligned} \quad (19)$$

Once the macroscopic variables at $\mathbf{x}_S - \mathbf{e}_i \delta t$ are obtained, the equilibrium pressure distribution functions $f_i^{eq}(\mathbf{x}_S - \mathbf{e}_i \delta t, t)$, the auxiliary equilibrium pressure distribution functions $f_i^{eq-m}(\mathbf{x}_S - \mathbf{e}_i \delta t, t)$, and the equilibrium volume fraction distribution functions $g_i^{eq}(\mathbf{x}_S - \mathbf{e}_i \delta t, t)$ are respectively calculated by

$$\begin{aligned} f_i^{eq} &= w_i [p + \rho \Gamma(u_\alpha)] \\ &= w_i \left\{ p + \rho c_s^2 \left[\frac{e_{i\alpha} u_\alpha}{c_s^2} + \frac{(e_{i\alpha} u_\alpha)^2}{2c_s^4} - \frac{u_\alpha u_\alpha}{2c_s^2} \right] \right\}, \end{aligned} \quad (20)$$

$$f_i^{eq-m}(\mathbf{x} - \mathbf{e}_i \delta t) = w_i \{ p(\mathbf{x} - \mathbf{e}_i \delta t) + \rho(\mathbf{x}) \Gamma[u_\alpha(\mathbf{x} - \mathbf{e}_i \delta t)] \}, \quad (21)$$

$$g_i^{eq} = \begin{cases} w_i (A \mu_C + C \frac{e_{i\alpha} u_\alpha}{c_s}), & i \neq 0 \\ C - A \mu_C + w_0 A \mu_C, & i = 0 \end{cases} \quad (22)$$

where Γ is a function of u_α defined in Eq. (20), A is an adjustable parameter, c_s is the sound speed, and $c_s^2 = c^2/3$ for the present D2Q9 and D3Q19 models. In the present paper, $A = M_C/(0.5c_s^2 \delta t)$ is adopted for all cases.

(c) Calculation of the equilibrium distribution functions at $(\mathbf{x}_S, t + \delta t)$: The streaming process of the lattice Boltzmann model is implemented to get the distribution functions

$$f_i(\mathbf{x}_S, t + \delta t) = f_i^{eq}(\mathbf{x}_S - \mathbf{e}_i \delta t, t), \quad (23)$$

$$g_i(\mathbf{x}_S, t + \delta t) = g_i^{eq}(\mathbf{x}_S - \mathbf{e}_i \delta t, t). \quad (24)$$

The predicted variables at $(\mathbf{x}_S, t + \delta t)$ are determined by

$$p^* = \sum_i f_i(\mathbf{x}_S, t + \delta t) = \sum_i f_i^{eq}(\mathbf{x}_S - \mathbf{e}_i \delta t, t), \quad (25)$$

$$\rho^* u_\alpha^* c_s^2 = \sum_i f_i(\mathbf{x}_S, t + \delta t) e_{i\alpha} = \sum_i f_i^{eq}(\mathbf{x}_S - \mathbf{e}_i \delta t, t) e_{i\alpha}, \quad (26)$$

$$C^* = \sum_i g_i(\mathbf{x}_S, t + \delta t) = \sum_i g_i^{eq}(\mathbf{x}_S - \mathbf{e}_i \delta t, t), \quad (27)$$

$$\mu_C^*(\mathbf{x}_S, t + \delta t) = \sum_i w_i \mu_C(\mathbf{x}_S - \mathbf{e}_i \delta t, t). \quad (28)$$

$f_i^{eq}(\mathbf{x}_S, t + \delta t)$ and $g_i^{eq}(\mathbf{x}_S, t + \delta t)$ thus can be determined by the predicted variables through Eqs. (20) and (22), respectively.

(d) Calculation of the interface fluxes:

$$R_\alpha = \sum_i f_i^{eq}(\mathbf{x}_S, t + \delta t) e_{i\alpha}, \quad (29)$$

$$\begin{aligned} \Pi_{\alpha\beta} &= \sum_i \{ f_i^{eq}(\mathbf{x}_S, t + \delta t) - (\tau_f - 0.5) [f_i^{eq}(\mathbf{x}_S, t + \delta t) \\ &- f_i^{eq-m}(\mathbf{x}_S - \mathbf{e}_i \delta t, t)] \} e_{i\alpha} e_{i\beta}, \end{aligned} \quad (30)$$

$$\begin{aligned} Q_\alpha &= \sum_i \{ g_i^{eq}(\mathbf{x}_S, t + \delta t) - (\tau_g - 0.5) [g_i^{eq}(\mathbf{x}_S, t + \delta t) \\ &- g_i^{eq}(\mathbf{x}_S - \mathbf{e}_i \delta t, t)] \} e_{i\alpha}, \end{aligned} \quad (31)$$

where τ_f is the relaxation time related to the kinematic viscosity

$$\nu = \frac{\mu}{\rho} = (\tau_f - 0.5) c_s^2 \delta t, \quad (32)$$

τ_g is the relaxation time related to the constant mobility

$$M_C = (\tau_g - 0.5) A c_s^2 \delta t. \quad (33)$$

III. CONSTRUCTION OF RMLBFS

In this section, MEs-MLBFS are derived in part A, while RMLBFS is constructed in part B.

A. MEs-MLBFS

By using the second-order Taylor series expansion, $f_i^{eq}(\mathbf{x}_S - \mathbf{e}_i \delta t, t)$ and $g_i^{eq}(\mathbf{x}_S - \mathbf{e}_i \delta t, t)$ can be expanded as

$$\begin{aligned} f_i^{eq}(\mathbf{x}_S - \mathbf{e}_i \delta t, t) &= f_i^{eq} - e_{i\alpha} \delta t \partial_\alpha f_i^{eq} + 0.5 \delta t^2 e_{i\alpha} e_{i\beta} \partial_\alpha \partial_\beta f_i^{eq} \\ &+ O(\delta t^3), \end{aligned} \quad (34)$$

$$\begin{aligned} g_i^{eq}(\mathbf{x}_S - \mathbf{e}_i \delta t, t) &= g_i^{eq} - e_{i\alpha} \delta t \partial_\alpha g_i^{eq} + 0.5 \delta t^2 e_{i\alpha} e_{i\beta} \partial_\alpha \partial_\beta g_i^{eq} \\ &+ O(\delta t^3). \end{aligned} \quad (35)$$

The equilibrium distribution functions f_i^{eq} and g_i^{eq} satisfy

$$\sum_i f_i^{eq} = p, \quad \sum_i f_i^{eq} e_{i\alpha} = \rho u_\alpha c_s^2,$$

$$\sum_i f_i^{eq} e_{i\alpha} e_{i\beta} = \rho c_s^2 \delta_{\alpha\beta} + \rho c_s^2 u_\alpha u_\beta,$$

$$\sum_i f_i^{eq} e_{i\alpha} e_{i\beta} e_{i\gamma} = \rho c_s^4 (u_\alpha \delta_{\beta\gamma} + u_\beta \delta_{\alpha\gamma} + u_\gamma \delta_{\alpha\beta}), \quad (36)$$

$$\sum_i g_i^{eq} = C, \quad \sum_i g_i^{eq} e_{i\alpha} = u_\alpha C, \quad \sum_i g_i^{eq} e_{i\alpha} e_{i\beta} = A \mu_C c_s^2 \delta_{\alpha\beta}. \quad (37)$$

Substituting Eqs. (34) and (36) into Eqs. (25) and (26), the predicted p and ρu_α at the interface are

$$\begin{aligned} p^* &= p^n - \partial_\alpha (\rho u_\alpha c_s^2) \delta t + \frac{1}{2} c_s^2 \delta t^2 \partial_\alpha \partial_\beta (\rho u_\alpha u_\beta + p \delta_{\alpha\beta}) \\ &+ O(\delta t^3), \end{aligned} \quad (38)$$

$$\begin{aligned} (\rho u_\alpha c_s^2)^* &= (\rho u_\alpha c_s^2)^n - c_s^2 \delta t \partial_\beta (\rho u_\alpha u_\beta + p \delta_{\alpha\beta}) \\ &+ 0.5 c_s^4 \delta t^2 \partial_\beta [\partial_\beta (\rho u_\alpha) + \partial_\alpha (\rho u_\beta) \\ &+ \partial_\gamma (\rho u_\gamma) \delta_{\alpha\beta}] + O(\delta t^3), \end{aligned} \quad (39)$$

where the superscripts n and $*$ denote the variables at time step n and the predicted variables, respectively. The predicted and updated variables are variables on interface centers at time $t + \delta t$ and cell centers at time $t + \Delta t$, respectively. Substituting Eqs. (35) and (37) into Eq. (27), the predicted C at the interface is

$$C^* = C^n - \delta t \partial_\alpha (u_\alpha C)^n + 0.5 A c_s^2 \delta t^2 \partial_\alpha \partial_\beta (\mu_C \delta_{\alpha\beta})^n + O(\delta t^3). \quad (40)$$

Similarly, the predicted μ_C at the interface is

$$\mu_C^* = \mu_C^n + 0.5 A c_s^2 \delta t^2 \partial_\alpha \partial_\beta (\mu_C \delta_{\alpha\beta})^n + O(\delta t^3). \quad (41)$$

By using the second-order Taylor series expansion,

$$\begin{aligned} f_i^{eq-m}(\mathbf{x}_S - \mathbf{e}_i \delta t, t) &= f_i^{eq-m} - e_{i\alpha} \delta t [w_i \partial_\alpha p + w_i \rho \partial_\alpha \Gamma_i(u_\alpha)] \\ &\quad + 0.5 e_{i\alpha} e_{i\beta} \delta t^2 [w_i \partial_\alpha \partial_\beta p \\ &\quad + w_i \rho \partial_\alpha \partial_\beta \Gamma_i(u_\alpha)] + O(\delta t^3). \end{aligned} \quad (42)$$

The auxiliary equilibrium distribution functions f_i^{eq-m} satisfy

$$\begin{aligned} \sum_i f_i^{eq-m} &= p, \quad \sum_i f_i^{eq-m} e_{i\alpha} = \rho u_\alpha c_s^2, \\ \sum_i f_i^{eq-m} e_{i\alpha} e_{i\beta} &= p c_s^2 \delta_{\alpha\beta} + \rho c_s^2 u_\alpha u_\beta, \\ \sum_i f_i^{eq-m} e_{i\alpha} e_{i\beta} e_{i\gamma} &= \rho c_s^4 (u_\alpha \delta_{\beta\gamma} + u_\beta \delta_{\alpha\gamma} + u_\gamma \delta_{\alpha\beta}). \end{aligned} \quad (43)$$

The auxiliary functions $\Gamma_i(u_\alpha)$ satisfy

$$\begin{aligned} \sum_i \Gamma_i(u_\alpha) &= 0, \quad \sum_i w_i \Gamma_i(u_\alpha) e_{i\alpha} = \rho u_\alpha c_s^2, \\ \sum_i w_i \Gamma_i(u_\alpha) e_{i\alpha} e_{i\beta} &= \rho u_\alpha u_\beta c_s^2, \\ \sum_i w_i \Gamma_i(u_\alpha) e_{i\alpha} e_{i\beta} e_{i\gamma} &= \rho c_s^4 (u_\alpha \delta_{\beta\gamma} + u_\beta \delta_{\alpha\gamma} + u_\gamma \delta_{\alpha\beta}). \end{aligned} \quad (44)$$

Substituting Eq. (36) into Eq. (29) leads to the pressure flux

$$R_\alpha = (\rho u_\alpha c_s^2)^*. \quad (45)$$

Substituting Eqs. (42), (43), and (44) into Eq. (30) leads to the momentum flux

$$\begin{aligned} \Pi_{\alpha\beta} &= \sum_i e_{i\alpha} e_{i\beta} \left\{ (1.5 - \tau_f) f_i^{eq}(\mathbf{x}_S, t + \delta t) + (\tau_f - 0.5) \right. \\ &\quad \times [f_i^{eq-m} - e_{i\gamma} \delta t (w_i \partial_\gamma p + w_i \rho \partial_\gamma \Gamma_i) + O(\delta t^2)] \left. \right\} \\ &= (\rho u_\alpha u_\beta c_s^2 + p \delta_{\alpha\beta} c_s^2)^* - \left\{ \rho v c_s^2 [\partial_\beta u_\alpha + \partial_\alpha u_\beta \right. \\ &\quad + \partial_\gamma u_\gamma \delta_{\alpha\beta}] \left. \right\}^n - (\tau_f - 0.5) [(\rho u_\alpha u_\beta c_s^2 + p c_s^2 \delta_{\alpha\beta})^* \\ &\quad - (\rho u_\alpha u_\beta c_s^2 + p c_s^2 \delta_{\alpha\beta})^n] + O(\delta t^2), \end{aligned} \quad (46)$$

where $v = (\tau_f - 0.5) c_s^2 \delta t$. Substituting Eqs. (35) and (37) into Eq. (31) leads to the volume fraction flux

$$\begin{aligned} Q_\alpha &= \sum_i e_{i\alpha} \left\{ g_i^{eq}(\mathbf{x}_S, t + \delta t) - (\tau_g - 0.5) [g_i^{eq}(\mathbf{x}_S, t + \delta t) \right. \\ &\quad - g_i^{eq}(\mathbf{x}_S, t) + e_{i\beta} \delta t \partial_\beta g_i^{eq}(\mathbf{x}_S, t) + O(\delta t^2)] \left. \right\} \\ &= (u_\alpha C)^* - M_C (\partial_\alpha \mu_C)^n - (\tau_g - 0.5) [(u_\alpha C)^* - (u_\alpha C)^n] \\ &\quad + O(\delta t^2), \end{aligned} \quad (47)$$

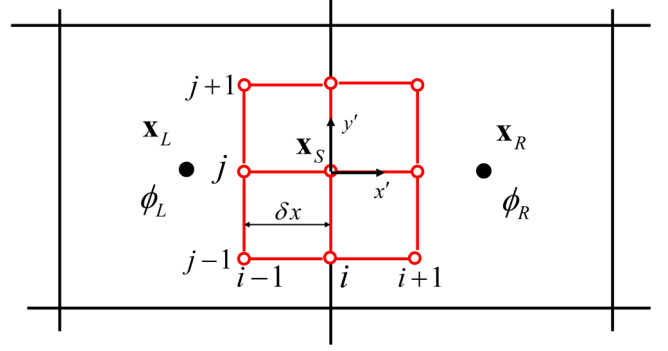


FIG. 2. The reconstructed unit lattice at the interface.

where $M_C = (\tau_g - 0.5) A c_s^2 \delta t$. Substituting Eqs. (45), (46), and (47) into Eqs. (12), (13), and (14), respectively, we can obtain the macroscopic equations of the corrector step

$$\partial_t p = -\partial_\alpha (\rho u_\alpha c_s^2)^* + u_\alpha \partial_\alpha (\rho c_s^2), \quad (48)$$

$$\begin{aligned} \partial_t (\rho u_\alpha c_s^2) &= -c_s^2 \partial_\beta (\rho u_\alpha u_\beta + p \delta_{\alpha\beta}) + \rho v c_s^2 \partial_\beta [\partial_\beta u_\alpha + \partial_\beta u_\alpha \\ &\quad + \partial_\gamma u_\gamma \delta_{\alpha\beta}] + (\tau_f - 1.5) c_s^2 [\partial_\beta (\rho u_\alpha u_\beta + p \delta_{\alpha\beta})^* \\ &\quad - \partial_\beta (\rho u_\alpha u_\beta + p \delta_{\alpha\beta})], \end{aligned} \quad (49)$$

$$\begin{aligned} \partial_t C &= -\partial_\alpha (u_\alpha C) + M_C \partial_\alpha \partial_\beta (\mu_C \delta_{\alpha\beta}) \\ &\quad + (\tau_g - 1.5) [\partial_\alpha (u_\alpha C)^* - \partial_\alpha (u_\alpha C)]. \end{aligned} \quad (50)$$

In the present paper, Eqs. (38), (39), (40), (48), (49), and (50) are labeled by MES-MLBFS.

B. RMLBFS

By directly solving MES-MLBFS with the finite volume scheme, RMLBFS can be constructed. It should be noted that MLBFS uses the staggered mesh where the predictor and corrector steps are implemented on the reconstructed unit lattice at the interface and cell centers, respectively. It has been proven that it is essential to restrain pressure oscillation for incompressible single-phase flows [28] (can be considered as special cases in multiphase flows). Therefore, the staggered mesh is also adopted for RMLBFS. Referring to the discretization scheme of MLBFS, RMLBFS is also solved through the predictor and corrector steps. The illustration is based on a 2D case. The computational procedures of interface fluxes can be summarized as follows.

(a) A unit lattice illustrated in Fig. 2 is reconstructed as well. Note that the local coordinate is adopted for the reconstructed unit lattice to ensure the lattice symmetry about the interface. Then the variables at the nine lattice nodes are interpolated by Eqs. (17), (18), and (19).

(b) Predictor step: Equations (38)–(41) without $O(\delta t^2)$ are discretized on the unit lattice by the least-squares finite difference method to obtain the predicted variables p^* , u_α^* , C^* , and μ_C^* at the interface. The detailed discretization scheme of the least-squares finite difference method can be found in Ref. [29].

(c) Corrector step: The interface fluxes at cell centers can be obtained by

$$R_\alpha = (\rho u_\alpha c_s^2)^*, \quad (51)$$

$$\begin{aligned} \Pi_{\alpha\beta} = & c_s^2 (\rho u_\alpha u_\beta + \rho c_s^2 \delta_{\alpha\beta})^n - \rho \nu c_s^2 [\partial_\beta u_\alpha + \partial_\beta u_\alpha \\ & + \partial_\gamma u_\gamma \delta_{\alpha\beta}]^n - (\tau_f - 1.5) c_s^2 [(\rho u_\alpha u_\beta + p \delta_{\alpha\beta})^* \\ & - (\rho u_\alpha u_\beta + p \delta_{\alpha\beta})^n], \end{aligned} \quad (52)$$

$$Q_\alpha = (u_\alpha C)^n - M_C (\partial_\alpha \mu C)^n - (\tau_g - 1.5) [(u_\alpha C)^* - (u_\alpha C)^n]. \quad (53)$$

Then the variables can be updated by solving Eqs. (48) to (50). Note that since the discretization scheme is of second-order accuracy, RMLBFS is a second-order approximation of MLBFS.

IV. THE REASON FOR THE GOOD NUMERICAL STABILITY OF MLBFS

Since MLBFS simulates incompressible multiphase flows by using the weakly compressible model, MLBFS should introduce some additional treatments to achieve good numerical stability. Therefore, this section analyzes the reason for the good numerical stability of MLBFS.

It can be seen from MEs-MLBFS that for $\delta t = 0$, MEs-MLBFS degenerate to

$$\partial_t p + \rho c_s^2 \partial_\alpha u_\alpha = 0, \quad (54)$$

$$\begin{aligned} \partial_t (\rho u_\alpha c_s^2) = & - \partial_\beta (\rho u_\alpha u_\beta c_s^2 + p c_s^2 \delta_{\alpha\beta}) \\ & + \mu c_s^2 \partial_\beta [\partial_\alpha u_\beta + \partial_\beta u_\alpha + u_\gamma \delta_{\alpha\beta}], \end{aligned} \quad (55)$$

$$\partial_t C = - \partial_\alpha (u_\alpha C) + \partial_\alpha [M_C \partial_\beta (\mu_C \delta_{\alpha\beta})], \quad (56)$$

which are the standard macroscopic governing equations, i.e., Eqs. (1), (2), and (3). In general, directly solving the weakly compressible model exhibits numerical instability.

When $\delta t \neq 0$, the predictor step of MEs-MLBFS introduces additional terms $0.5 c_s^2 \delta t \partial_\alpha \partial_\beta (\rho u_\alpha u_\beta + p \delta_{\alpha\beta})^n$ to the pressure equation and fixed viscous terms $0.5 c_s^4 \delta t^2 \partial_\beta [\partial_\beta (\rho u_\alpha) + \partial_\alpha (\rho u_\beta) + \partial_\gamma (\rho u_\gamma) \delta_{\alpha\beta}]^n$ to the momentum equation. The corrector step also includes some additional terms. The recovered macroscopic pressure and momentum equations of the corrector step in MEs-MLBFS are

$$\partial_t p = - \rho c_s^2 \partial_\alpha (u_\alpha) + c_s^2 \delta t \partial_\alpha \partial_\beta (\rho u_\alpha u_\beta + p \delta_{\alpha\beta}) + O(\delta t^2), \quad (57)$$

$$\begin{aligned} \partial_t (\rho u_\alpha c_s^2) = & - c_s^2 \partial_\beta (\rho u_\alpha u_\beta + p \delta_{\alpha\beta}) + \rho \nu c_s^2 \partial_\beta [\partial_\beta u_\alpha + \partial_\beta u_\alpha \\ & + \partial_\gamma u_\gamma \delta_{\alpha\beta}] + (\tau_f - 1.5) c_s^2 [\partial_\beta (\rho u_\alpha u_\beta)^* \\ & - \partial_\beta (\rho u_\alpha u_\beta)] + (1.5 - \tau_f) c_s^4 \delta t \partial_\alpha \partial_\beta (\rho u_\beta) \\ & + O(\delta t^2). \end{aligned} \quad (58)$$

It can be seen that for both the predictor and corrector steps, there are pressure diffusion terms related to $\partial_\alpha \partial_\beta (p \delta_{\alpha\beta})$ in the pressure equations and bulk viscosity terms related to $\partial_\alpha \partial_\beta u_\beta$

in the momentum equations. Note that the additional terms and the fixed viscous terms in the predictor step mentioned above, which correspond to the third-order partial derivatives in the corrector step, are included in $O(\delta t^2)$ terms here.

It has been proven that the pressure diffusion term is efficient to damp the pressure oscillations inherent to the weakly compressible model [30], and it is efficient to stabilize computations of both single-phase [30] and multiphase flows [31]. The viscous terms also contribute to damping the pressure oscillations. Numerical experiments [32] confirm that sound waves experience the correct dissipation due to the intended bulk and shear viscosities.

To investigate the effect of these dissipation terms in stabilizing computation, first, the stable droplet is simulated. In the computational domain $[-L/2, L/2] \times [-L/2, L/2]$, there is a liquid droplet of radius R_0 in the center while the remaining domain is filled with gas. To avoid the influence of the discretization scheme, the first-order explicit time discretization scheme is adopted for all models in the present section.

First, the numerical stability of three models, i.e., MLBFS, RMLBFS, and the nondissipative model which is RMLBFS at $\delta t = 0$, are investigated. The parameters of the liquid and gas are labeled by subscripts H and L , respectively. The fixed parameters include $\sigma = 0.001$, $\xi = 4$, $\rho_H = 1$, $\mu_H = 0.01$, $R_0 = 0.2L$, $M_C = 0.1$, $\delta t = 0.5$, $\Delta t = 0.5$ while the density ratio $R_\rho = \rho_H / \rho_L$ and viscosity ratio $R_\mu = \mu_H / \mu_L$ are both in a large range from 1 to 1000. A uniform mesh of size 200×200 is adopted for all test cases. Initially, the phase field is set as

$$C(x, y) = 0.5 - 0.5 \tanh[2(\sqrt{x^2 + y^2} - R_0)/\xi]. \quad (59)$$

Figure 3 shows that MLBFS and RMLBFS can get convergent results in a large range of R_ρ and R_μ . In contrast, the nondissipative model is divergent in all test cases. It can also be seen that the stable parameter range of RMLBFS matches well with that of MLBFS. The comparison indicates that the numerical dissipation terms involved in MLBFS are essential to stabilizing computation. Without these dissipation terms, the results are found to be unstable. On the contrary, with these numerical dissipation terms, good numerical stability at high density and dynamic viscosity ratios can be achieved by MLBFS and RMLBFS.

Furthermore, to confirm whether the numerical dissipation terms in the predictor step or the corrector step are the main reason for the good numerical stability, the numerical stability of the reduced RMLBFS, which removes the numerical dissipation terms in the predictor step of RMLBFS, is investigated. The macroscopic equations of the predictor step in the reduced RMLBFS are given as

$$p^* = p^n - \rho c_s^2 (\partial_\alpha u_\alpha)^n \delta t, \quad (60)$$

$$(\rho u_\alpha c_s^2)^* = (\rho u_\alpha c_s^2)^n - c_s^2 \delta t \partial_\beta (\rho u_\alpha u_\beta + p \delta_{\alpha\beta})^n, \quad (61)$$

$$C^* = C^n - \delta t \partial_\alpha (u_\alpha C)^n + 0.5 A c_s^2 \delta t^2 \partial_\alpha \partial_\beta (\mu_C \delta_{\alpha\beta})^n. \quad (62)$$

Compared with the macroscopic equations of the predictor step in RMLBFS, the second-order partial derivatives that contain the pressure diffusion and viscous terms are removed in Eqs. (60) to (62). The macroscopic equations of the cor-

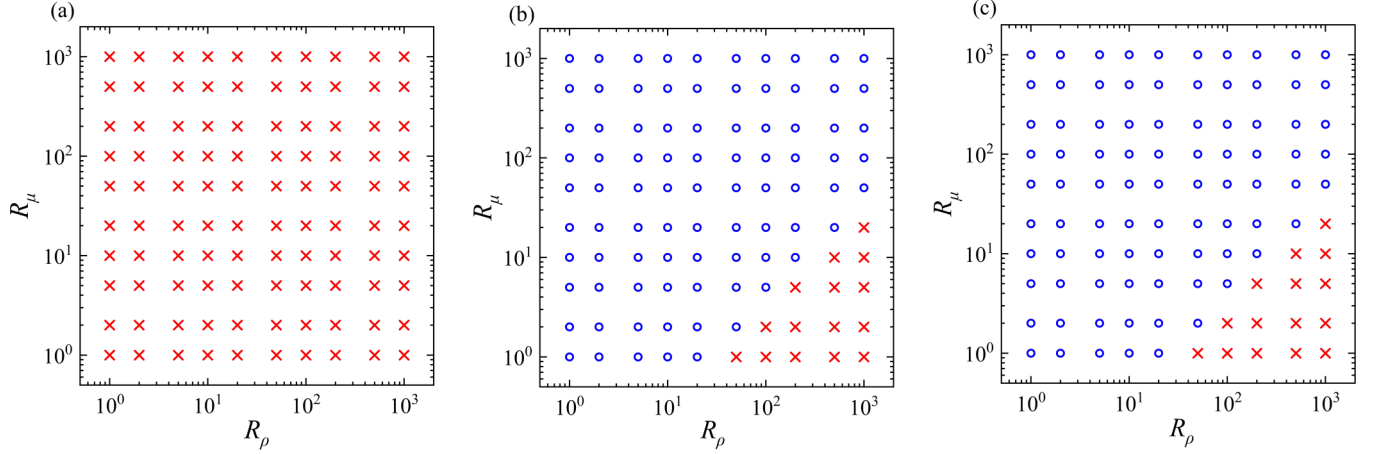


FIG. 3. Stability of MLBFS (a), RMLBFS (b), and the nondissipative model (c) for simulating a stable droplet in the gas. The blue circle indicates stable and the red cross indicates unstable solutions.

rector step in the reduced RMLBFS are the same as those of RMLBFS, i.e., Eqs. (51) to (53). The computational procedures and discretization scheme of the reduced RMLBFS follow those of RMLBFS. The corresponding macroscopic pressure and momentum equations of the reduced RMLBFS can be rewritten as

$$\partial_t p = -\rho c_s^2 \partial_\alpha (u_\alpha) + c_s^2 \delta t \partial_\alpha \partial_\beta (\rho u_\alpha u_\beta + p \delta_{\alpha\beta}), \quad (63)$$

$$\begin{aligned} \partial_t (\rho u_\alpha c_s^2) = & -c_s^2 \partial_\beta (\rho u_\alpha u_\beta + p \delta_{\alpha\beta}) + \rho \nu c_s^2 \partial_\beta [\partial_\beta u_\alpha + \partial_\beta u_\alpha \\ & + \partial_\gamma u_\gamma \delta_{\alpha\beta}] + (\tau_f - 1.5) c_s^2 [\partial_\beta (\rho u_\alpha u_\beta)^* \\ & - \partial_\beta (\rho u_\alpha u_\beta)] + \partial_\alpha [\rho (1.5 - \tau_f) c_s^4 \delta t \partial_\beta u_\beta]. \end{aligned} \quad (64)$$

The differences between the recovered macroscopic pressure and momentum equations of the corrector step in RMLBFS and the reduced RMLBFS are $O(\delta t^2)$ terms.

Figure 4 shows the convergence situations of the reduced RMLBFS at different R_ρ and R_μ . It can be seen that the

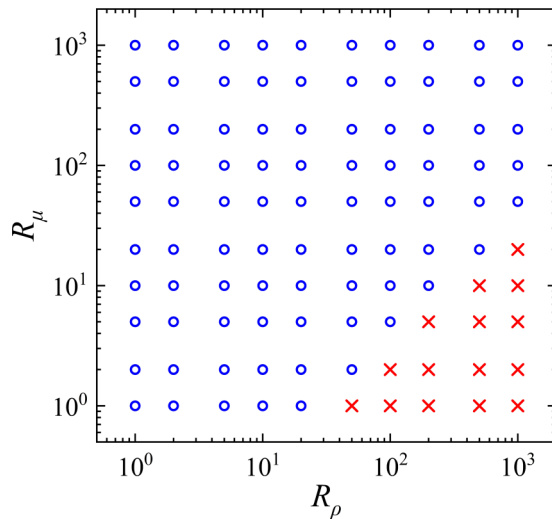


FIG. 4. Stability of the reduced RMLBFS. The blue circle indicates stable and the red cross indicates unstable solutions.

stable parameter range of the model is the same as those of MLBFS and RMLBFS. The result indicates that the numerical dissipation terms in the corrector step rather than the predictor step are the key point of stabilizing computation.

Furthermore, to test the numerical stability of MLBFS, RMLBFS, the nondissipative model (RMLBFS at $\delta t = 0$), and the reduced RMLBFS over a wide range of Reynolds numbers, 2D droplet splashing on a thin film is simulated by the four models. The physical model is depicted in Fig. 5. Initially, the liquid droplet of radius R is tangential to the liquid film surface and moves downward with a velocity U . The density and dynamic viscosity of the liquid droplet and the surrounding gas are denoted as (ρ_H, μ_H) and (ρ_L, μ_L) , respectively. This problem is characterized by the Reynolds number Re and the Weber number We . Their definitions are given as

$$Re = \frac{2\rho_H UR}{\mu_H}, \quad We = \frac{2\rho_H U^2 R}{\sigma}. \quad (65)$$

Since the case is symmetric, only a half domain needs to be simulated. A uniform mesh of size 1000×500 is adopted for all simulations. The fixed parameters are $U = 0.004$, $\delta t = 0.5$, $\Delta t = 0.3$, $R = 100$, $\rho_H = 1$, $\rho_H/\rho_L = 1000$, $\mu_H/\mu_L = 100$, and $We = 150$, while M_C is in the range from 2 to 1000, and Re is in the range from 20 to 5000. If the model can

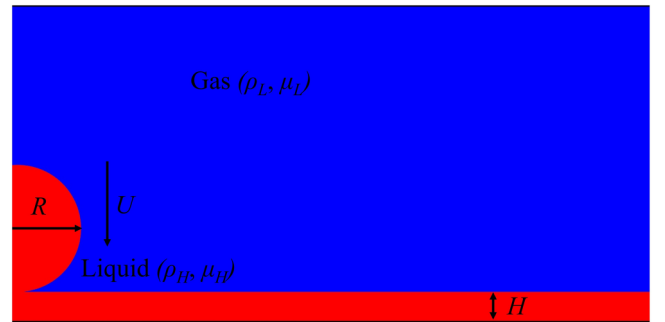


FIG. 5. Schematic diagram of the droplet splashing on a thin film.

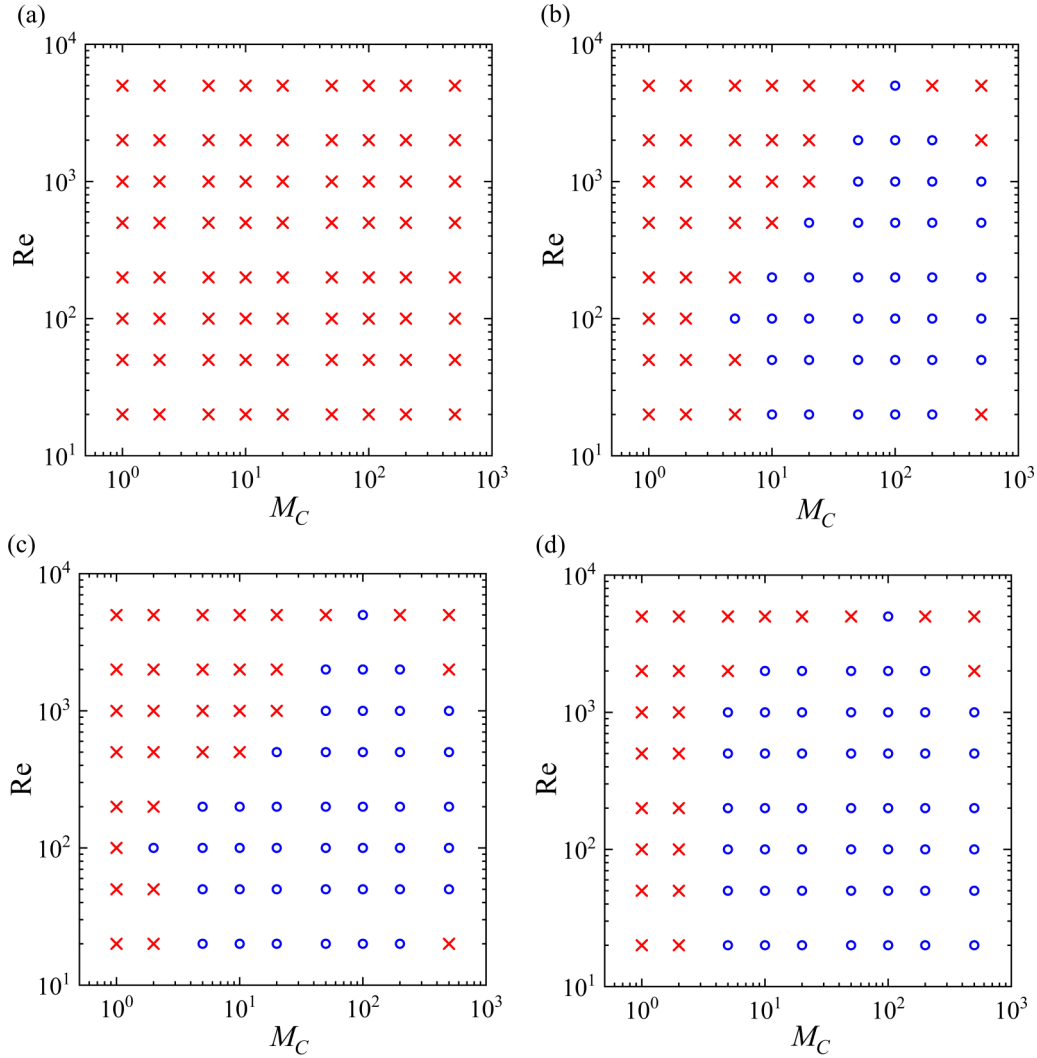


FIG. 6. Stability of the nondissipative model (a), MLBFS (b), RMLBFS (c), and the reduced RMLBFS (d) for simulating 2D droplet splashing on a thin liquid film. The blue circle indicates stable and the red cross indicates unstable solutions.

give a convergent result at $T = t\sqrt{g/d} = 2$, it is thought to be convergent.

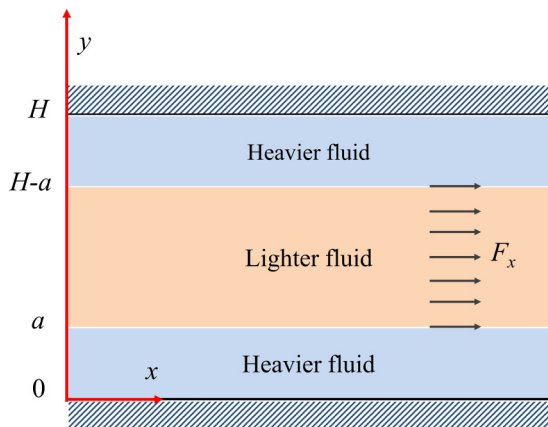


FIG. 7. Schematic diagram of the co-current flow.

The convergence situations of the four models are shown in Fig. 6. It can be seen that without those dissipation terms, the nondissipative model, i.e., RMLBFS with $\delta t = 0$, cannot obtain convergent results. On the contrary, MLBFS and RMLBFS with the pressure diffusion and bulk viscosity terms show obvious improvement in numerical stability. Besides, the reduced RMLBFS that does not have dissipation terms in the predictor step has similar numerical stability as RMLBFS. Once again, the result validates that it is the pressure diffusion and bulk viscosity terms in the corrector step that contribute to the good numerical stability of MLBFS.

V. NUMERICAL RESULTS AND DISCUSSIONS

To test RMLBFS further, six test cases are simulated by RMLBFS in this section. For better accuracy and numerical stability, the third-order Runge-Kuta scheme is adopted for the time discretization of RMLBFS for all cases in this section.

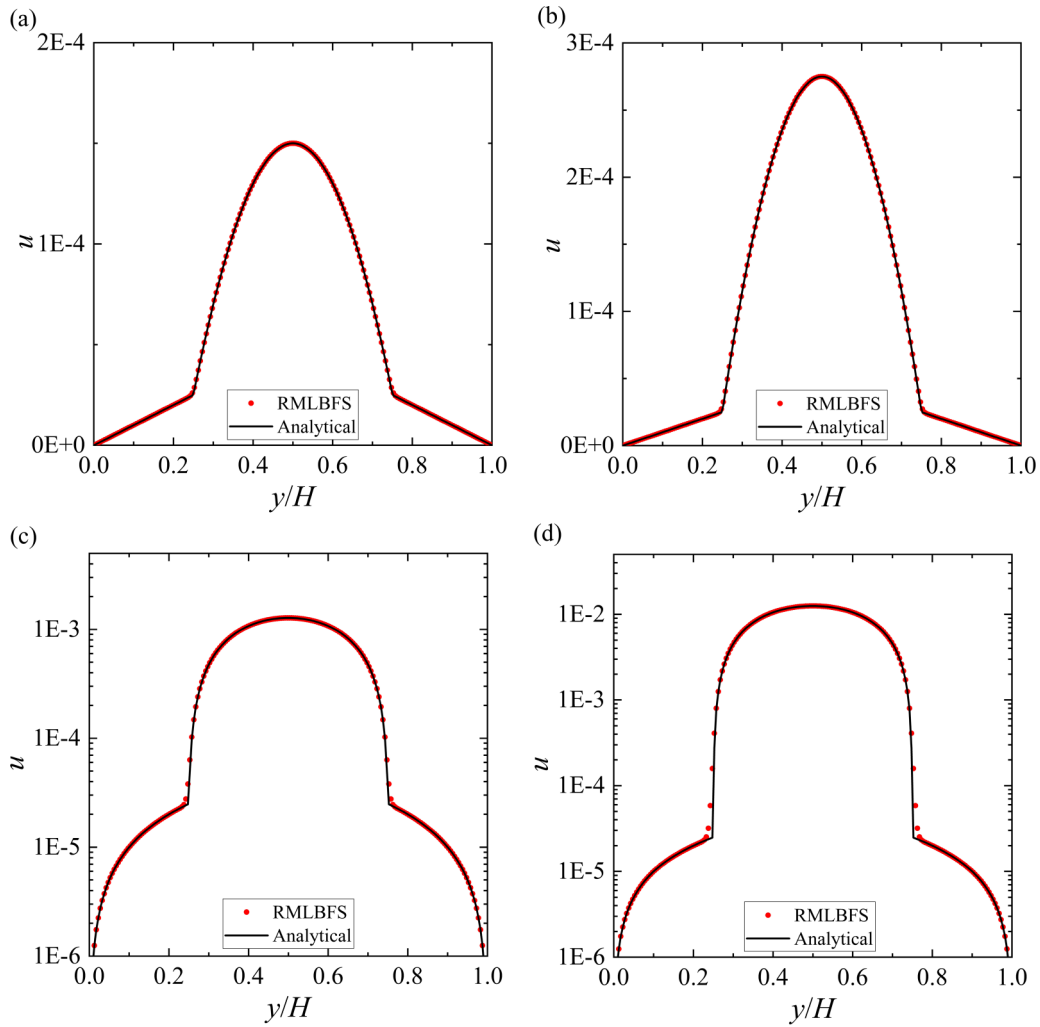


FIG. 8. Velocity profiles of the two-phase co-current flows at different density ratios. (a) $R_\rho = 10$, (b) $R_\rho = 20$, (c) $R_\rho = 100$, and (d) $R_\rho = 1000$.

A. Immiscible two-phase cocurrent flow in a 2D channel

To test the correctness of RMLBFS for multiphase flows with large density ratios, the immiscible two-phase cocurrent flow in a 2D channel driven by an external force F_x is

simulated. The schematic diagram of this case is displayed in Fig. 7. The area $|y - H/2| \leq H/2 - a$ is filled with the lighter fluid of density ρ_L and dynamic viscosity μ_L , while the area $H/2 - a < |y - H/2| \leq H/2$ is filled with the heavier

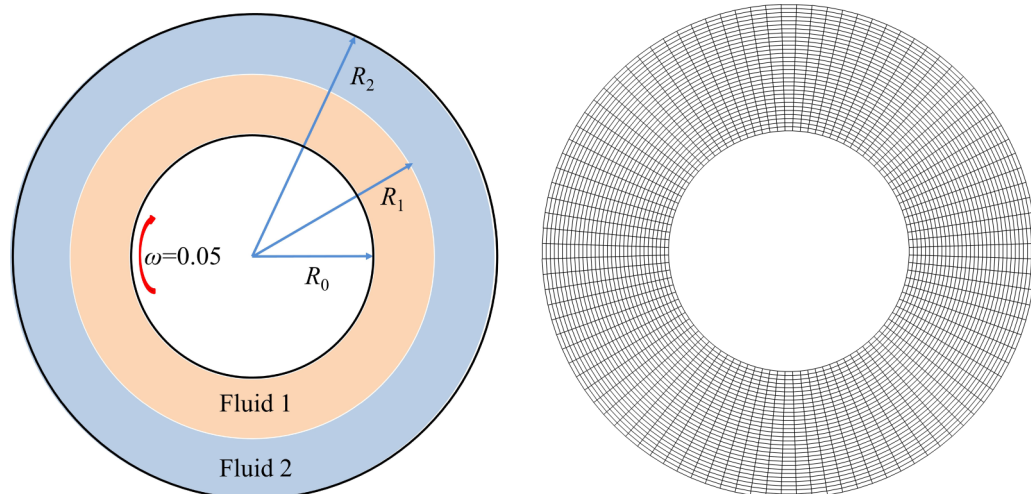


FIG. 9. Schematic diagram and the O-type computational mesh of the two-phase Taylor-Couette flows.

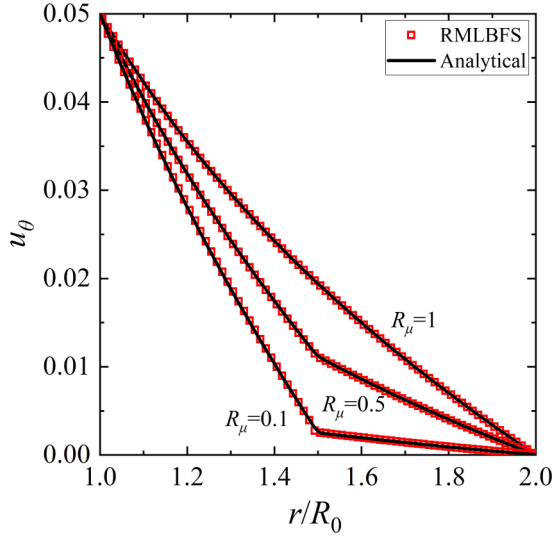


FIG. 10. Comparison of the azimuthal velocity profiles at different dynamic viscosity ratios for the two-phase Taylor-Couette flows in an annular area.

fluid of density ρ_H and dynamic viscosity μ_H . A constant force is imposed on the lighter fluid, and then the system would come to a steady state. The analytical steady solutions of the case are

$$u_a = \begin{cases} \left(-\frac{F_x a}{\mu_H} + \frac{F_x H}{2\mu_H}\right)y & 0 \leq y \leq a, \\ -\frac{F_x}{2\mu_L}y^2 + \frac{F_x H}{2\mu_L}y + \left(\frac{F_x a^2}{2\mu_L} - \frac{F_x a^2}{\mu_H} + \frac{F_x H a}{2\mu_H} - \frac{F_x H a}{2\mu_L}\right) & a < y \leq H - a, \\ -\left(-\frac{F_x a}{\mu_H} + \frac{F_x H}{2\mu_H}\right)(H - y) & H - a < y \leq H. \end{cases} \quad (66)$$

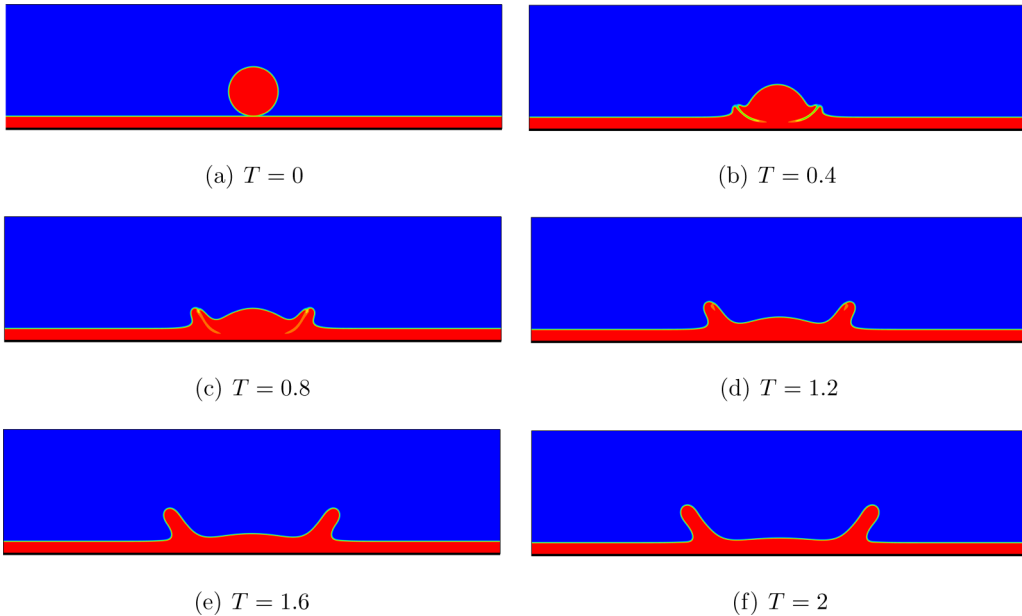


FIG. 11. Evolution of the fluid interface for droplet splashing on a thin liquid film at $Re = 100$.

Four different density ratios, $R_\rho = \rho_H/\rho_L = 10, 20, 100,$ and 1000 , are considered. Other parameters are set as $\nu_H = \nu_L = 0.01$, $a = 0.25H$, $\rho_H = 1$, and $F_x = 10^{-9}$. A fine uniform grid of size 3×200 is applied for the four cases. Figure 8 shows the velocity profiles at different density ratios. It is seen that the results given by RMLBFS agree very well with the corresponding analytical solutions, which verifies the correctness of RMLBFS for steady multiphase flows with large density ratios.

B. Two-phase Taylor-Couette flow in an annular area

To show the advantage of RMLBFS in tackling curved boundary, the two-phase Taylor-Couette flow in an annular area is considered. The physical model and O-typical body-fitted mesh used for simulation are depicted in Fig. 9. The annulus is filled with two fluids, fluid 1 in the area $R_0 \leq r \leq R_1$ and fluid 2 in the area $R_1 < r \leq R_2$. The inner boundary of radius R_0 has a fixed angular velocity ω , while the outer boundary of radius R_2 is stationary. The steady velocity field is determined by the dynamic viscosity ratio denoted by $R_\mu = \mu_1/\mu_2$ where μ_1 and μ_2 are the dynamic viscosities of fluid 1 and fluid 2, respectively. The corresponding analytical solutions for this problem at a low Reynolds number are

$$u_\theta = \begin{cases} A_1 r + B_1/r & r \leq R_1, \\ A_2 r + B_2/r & r \geq R_1, \end{cases} \quad (67)$$

where

$$A_1 = \frac{\omega \left[R_\mu \left(\frac{R_0^2}{R_2^2} - \frac{R_0^2}{R_1^2} \right) + \frac{R_0^2}{R_1^2} \right]}{R_\mu \left(\frac{R_0^2}{R_2^2} - \frac{R_0^2}{R_1^2} \right) + \left(\frac{R_0^2}{R_1^2} - 1 \right)},$$

$$B_1 = \frac{-\omega R_0^2}{R_\mu \left(\frac{R_0^2}{R_2^2} - \frac{R_0^2}{R_1^2} \right) + \left(\frac{R_0^2}{R_1^2} - 1 \right)},$$

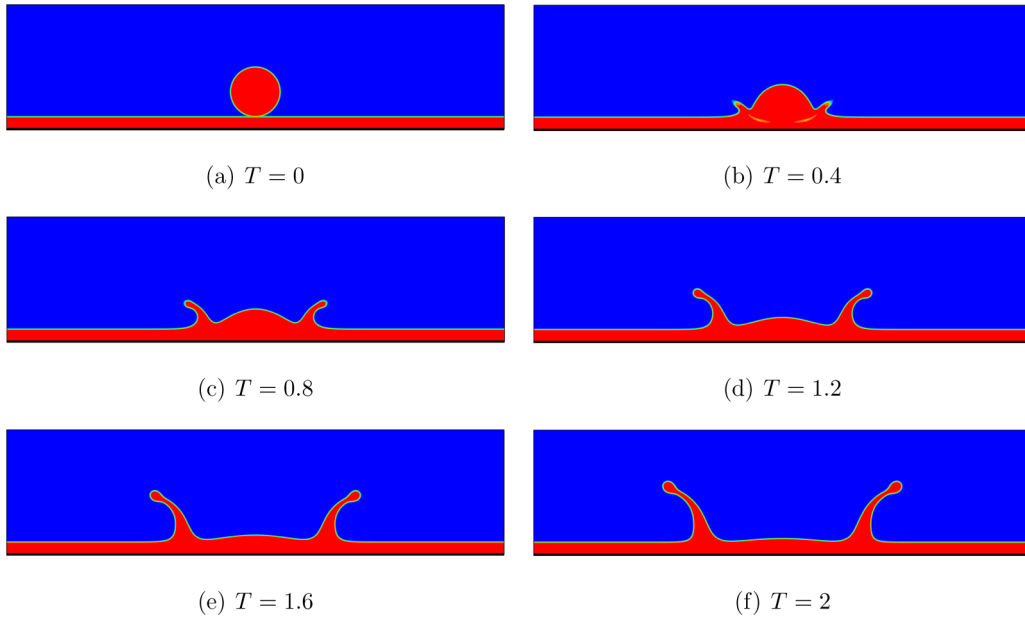


FIG. 12. Evolution of the fluid interface for droplet splashing on a thin liquid film at $Re = 400$.

$$A_2 = \frac{R_\mu \frac{R_0^2}{R_2^2} \omega}{R_\mu \left(\frac{R_0^2}{R_2^2} - \frac{R_0^2}{R_1^2} \right) + \left(\frac{R_0^2}{R_1^2} - 1 \right)},$$

$$B_2 = \frac{-R_\mu \omega R_0^2}{R_\mu \left(\frac{R_0^2}{R_2^2} - \frac{R_0^2}{R_1^2} \right) + \left(\frac{R_0^2}{R_1^2} - 1 \right)}.$$

In the present simulation, a nonuniform mesh of size 160×80 is adopted, and the parameters are set as $R_0 = 1, R_1 = 1.5, R_2 = 2, \omega = 0.05$. Three different viscosity ratios, $R_\mu = 1, 0.5$, and 0.1 , are tested. The inside and outside cylinder surfaces are set as the no-slip boundary condition. Figure 10 shows the comparison between the results given by RMLBFS

and the analytical solutions. It can be seen that the present results at different dynamic viscosity ratios always agree well with the corresponding analytical solutions, which proves the flexibility of RMLBFS for the application on nonuniform meshes.

C. 2D droplet splashing on a thin film

To validate RMLBFS for multiphase flows with large density ratios and high Reynolds numbers, 2D droplet splashing on a thin film with large density ratios and high Reynolds numbers is simulated in this section. The previous study of this problem [33] shows that the impact radius is an exponen-

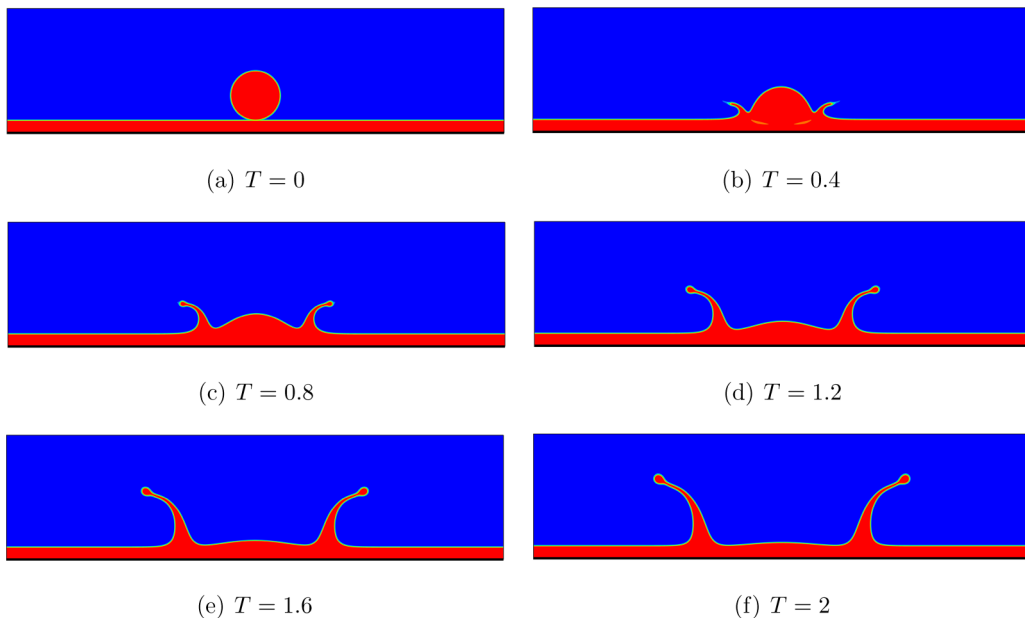


FIG. 13. Evolution of the fluid interface for droplet splashing on a thin liquid film at $Re = 1000$.

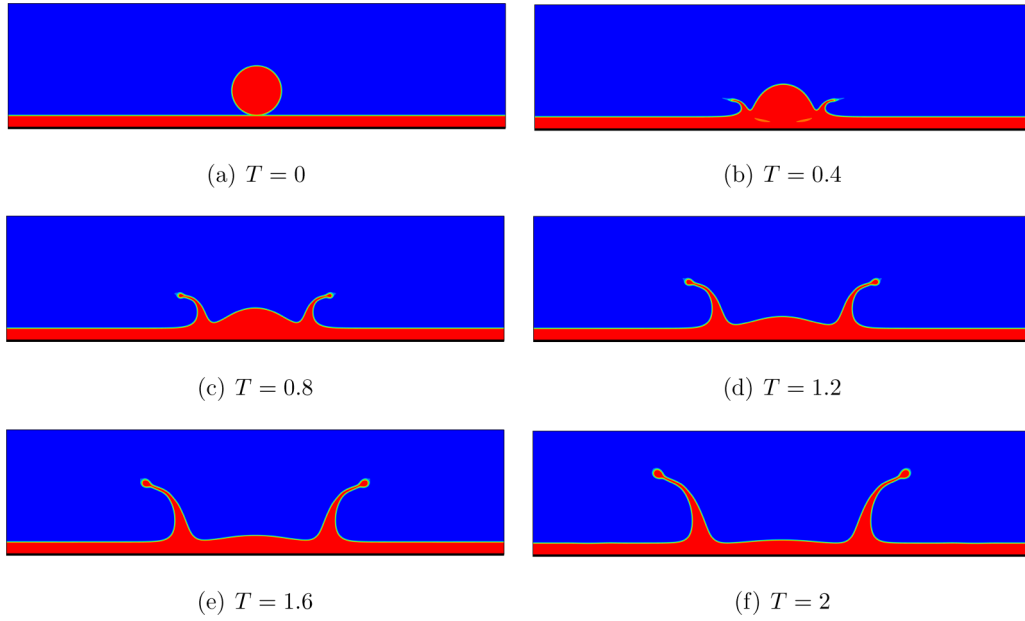


FIG. 14. Evolution of the fluid interface for droplet splashing on a thin liquid film at $Re = 2000$.

tial function of time. This law has also been validated by the research of Li *et al.* [11], Wang *et al.* [19], and Li *et al.* [23].

The schematic diagram of this problem is depicted in Fig. 5, and the detailed description can be seen in Sec. IV. A uniform mesh of size 1000×500 is adopted for all simulations. Other parameters are set as $U = 0.004$, $R = 100$, $\rho_H = 1$, $\rho_H/\rho_L = 1000$, $\mu_H/\mu_L = 100$, $We = 150$, while four different Reynolds numbers 100, 400, 1000, and 2000 are considered to validate RMLBFS for large density ratios and high Reynolds numbers.

The transient phase fields for $Re = 100, 400, 1000$, and 2000 are shown in Figs. 11–14, respectively. It can be seen that as the droplet hits the liquid film, the droplet deforms and tends to spread. The tendency is hindered by the surrounding liquid film, and thus the droplet periphery spreads outward

and is pushed upward by the surrounding film simultaneously. When the Reynolds number is relatively low ($Re = 100$), an outward-moving surface wave can be observed from Fig. 11, and the splashing is not obvious. As the Reynolds number increases, obvious liquid splashing can be observed.

To quantify the present results, the transient dimensionless impact radius is investigated. The impact radius is defined as the distance from the intersection of the unperturbed droplet and the unperturbed surface of the liquid layer to the origin [33]. The transient dimensionless impact radius approximately satisfies the power law $r/(2R) \approx A\sqrt{Ut/(2R)}$, where A is a constant of about 1.0 according to the theoretical predictions [33]. The regularity has also been verified by Wang *et al.* [19] and Li *et al.* [23]. The transient dimensionless impact radii at different Reynolds numbers as a function of $Ut/(2R)$ are given in Fig. 15. It can be seen that the present numerical results roughly satisfy the prediction of the power law, which confirms the correctness of RMLBFS for large density ratios and Reynolds numbers.

D. 2D Rayleigh-Taylor instability

In this section, the 2D Rayleigh-Taylor instability problem is simulated to further validate RMLBFS for multiphase flows with complex interface evolution. The Rayleigh-Taylor instability of two fluids under gravity involves complex interface evolution and has been widely investigated [7,19,23]. In this problem, the heavier fluid of density ρ_H floats on a lighter fluid of density ρ_L . If the interface is perturbed, such as small changes of pressure gradient and interface curvature, the interface would collapse owing to the influence of gravity, which is called Rayleigh-Taylor instability.

The computational domain is set as $-d/2 \leq x \leq d/2, 0 \leq y \leq 4d$. The left and right boundaries are periodic, while the upper and lower boundaries are set as the nonslip condition. The problem is characterized by two dimensionless numbers, i.e., the Reynolds number Re and the Atwood number At .

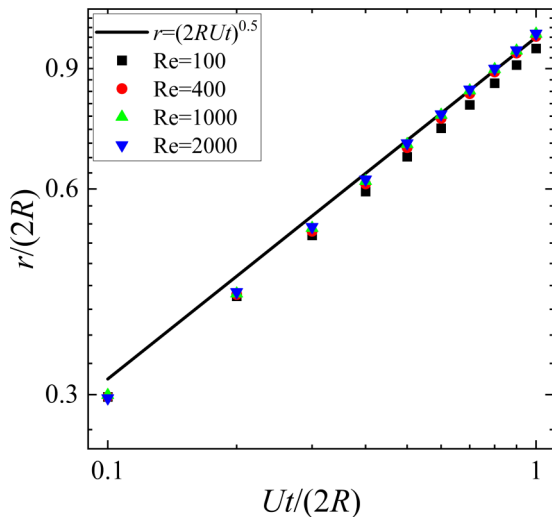


FIG. 15. The transient impact radii at different Reynolds numbers for droplet splashing on a thin film.

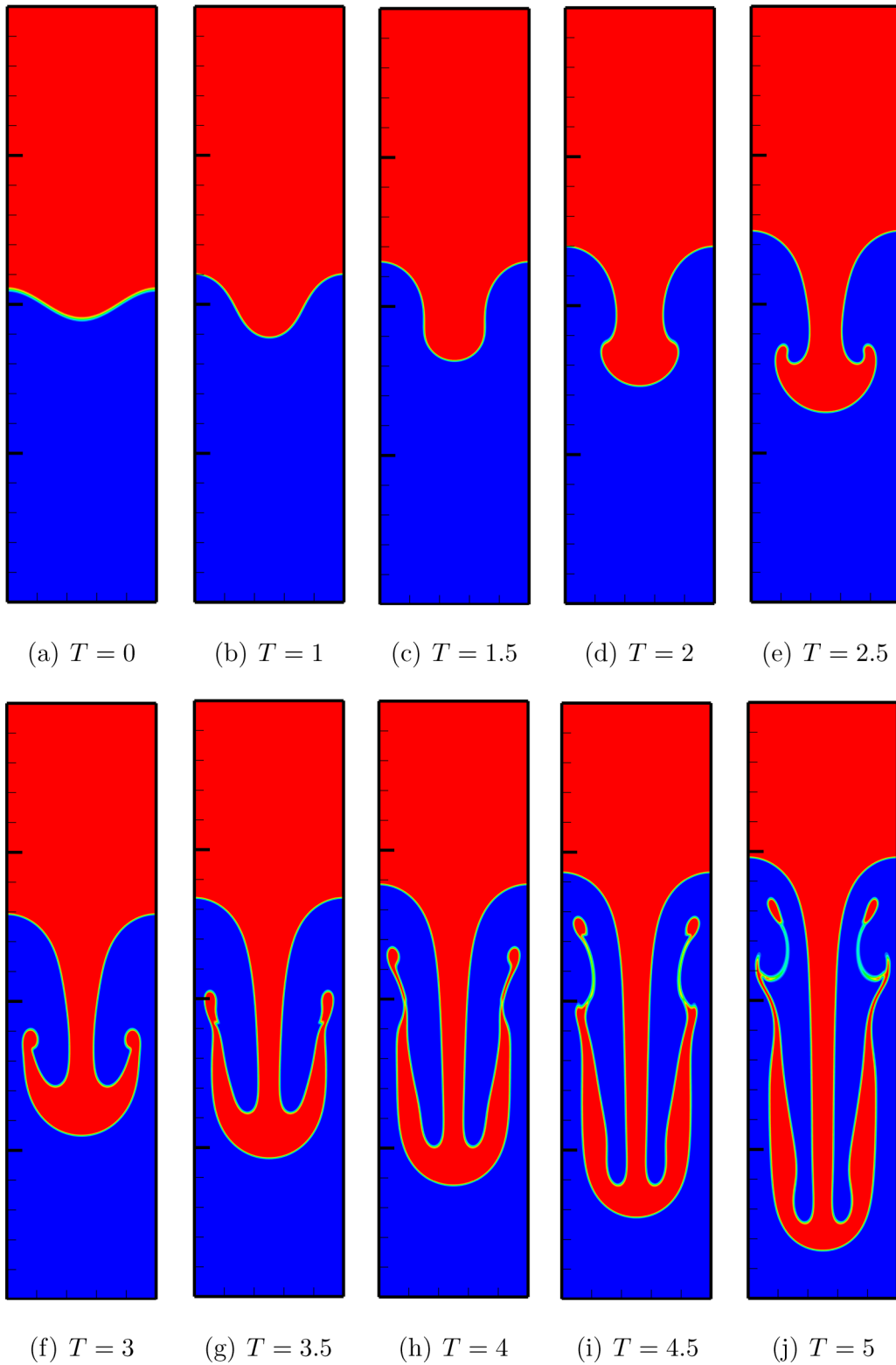


FIG. 16. Evolution of the fluid interface for the 2D Rayleigh-Taylor instability problem at $Re = 256$.

They are respectively defined as

$$Re = \frac{\sqrt{dg} \cdot d}{\nu}, \quad At = \frac{\rho_H - \rho_L}{\rho_H + \rho_L}, \quad (68)$$

where d is the characteristic length. Note that the two fluids have identical kinematic viscosity ν . Initially, the perturbed

interface is given as

$$y(x) = 2d + 0.1d \cos(2\pi x/d). \quad (69)$$

In the present simulation, a uniform mesh of size 200×800 is adopted, $At = 0.5$ is fixed, and two different Reynolds numbers, 256 and 2048, are considered. Other simulation

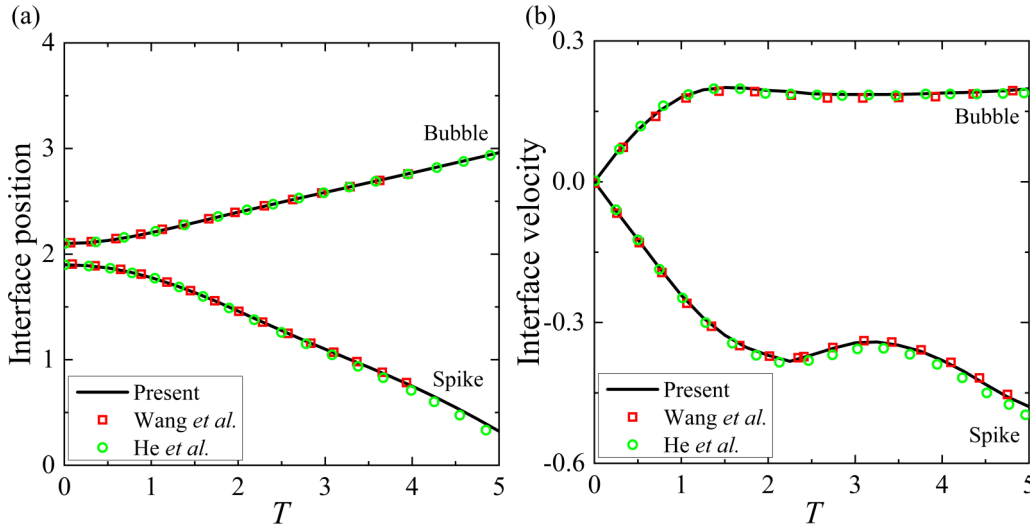


FIG. 17. Positions and velocities of the spike tip and bubble front for the 2D Rayleigh-Taylor instability problem at $Re = 256$, together with those given by Wang *et al.* [19] and He *et al.* [7].

parameters are set as $\rho_L = 1$ and $\sqrt{dg} = 0.01$. Note that the time and interface velocity are nondimensionalized, and they are defined as $T = t\sqrt{g/d}$ and v/\sqrt{dg} , respectively.

The results at $Re=256$ are discussed firstly. Figure 16 shows the transient interfaces at different times. It can be seen that at the early stage, the central heavy fluid falls to form a spike and the lighter fluid at the two sides rises to form bubbles. At $T = 2$, two symmetric roll-ups occur at the spike. As the evolution continues, the two roll-ups stretch upward, and a pair of secondary vortices appear at the tails of the roll-ups. All these observations are in good accordance with those reported in Refs. [7,19,23]. To quantify and validate the present results, the positions and velocities of the spike tip and bubble front obtained by RMLBFS are compared to those of Wang *et al.* [19] using MLBFS and He *et al.* [7] using a phase-field-based lattice Boltzmann method. As shown in Fig. 17, good agreement can be observed between the present results and the reference data [7,19].

As to the results at $Re = 2048$, it can be seen from Fig. 18 that similar phenomena, like roll-ups and secondary vortices at $Re = 256$, can also be observed. However, the interface shows more complex evolution and interface breakup exists. The evolution of the interface also matches well those given by He *et al.* [7]. Also, the positions and velocities of the spike tip and bubble front given by RMLBFS are compared with the results given by He *et al.* [7] in Fig. 19. Good agreement can be observed as well. These comparisons validate the ability of RMLBFS to stimulate transient multiphase flows with complex interface evolution.

E. 3D Rayleigh-Taylor instability

To show the generality of RMLBFS for both 2D and 3D situations, the 3D unsteady Rayleigh-Taylor instability problem is simulated. The problem is characterized by two nondimensional parameters, the Reynolds number Re and the Atwood number At defined as Eq. (68) as well.

In the present study, the computational domain is set as $-d/2 \leq x \leq d/2$, $-d/2 \leq y \leq d/2$, $0 \leq z \leq 4d$. The four

vertical boundaries are periodic, and the upper and lower walls are set as the no-slip boundary condition. A uniform mesh of size $128 \times 128 \times 512$ is adopted for simulation. The computational parameters are set as $\sqrt{dg} = 0.02$, $\rho_L = 1$, $At = 0.5$, and $Re = 1024$. Initially, the interface is perturbed by

$$\frac{h(x, y)}{d} = 2d + 0.05d \left[\cos\left(\frac{2\pi x}{d}\right) + \cos\left(\frac{2\pi y}{d}\right) \right]. \quad (70)$$

Figure 20 shows the interface shape at different dimensionless times including $T = t\sqrt{g/d} = 1, 2, 3$, and 4. It can be seen that the interface stretches first and then roll-ups appear generally. The lighter fluid rises to form bubbles at the four corners, while the heavier fluid falls to generate a spike in the central area. Also, there are four saddle points at the middle of the four sides. These characteristics and the interface shapes at different times agree well with the results of He *et al.* [34] using the lattice Boltzmann method based on a phase-field model and Wang *et al.* [21] using MLBFS.

To validate the results of RMLBFS in quantity, the positions and velocities of the bubble front, spike tip, and saddle point obtained by RMLBFS are compared with the reference data [21,34,35] in Fig. 21. It can be seen that the transient interface positions match well the reference results of He *et al.* [34] using the lattice Boltzmann method based on a phase-field model, Wang *et al.* [21] using MLBFS, Lee and Kim [35] using a projection method. The transient velocities are in good accordance with the reference results of Wang *et al.* [21] using MLBFS. These results verify the ability of RMLBFS for simulating 3D transient multiphase flows with complex interface evolution.

F. 3D head-on collisions of binary microdroplets

To test RMLBFS for 3D multiphase flows with large density ratios, head-on collisions of binary microdroplets are simulated. The two droplets in the gas have the same diameter D and opposite velocity of $U/2$. The computational domain is $-3D \leq x \leq 3D$, $-1.5D \leq y \leq 1.5D$, $-1.5D \leq z \leq 1.5D$. On all outside boundaries, Neumann boundary conditions of

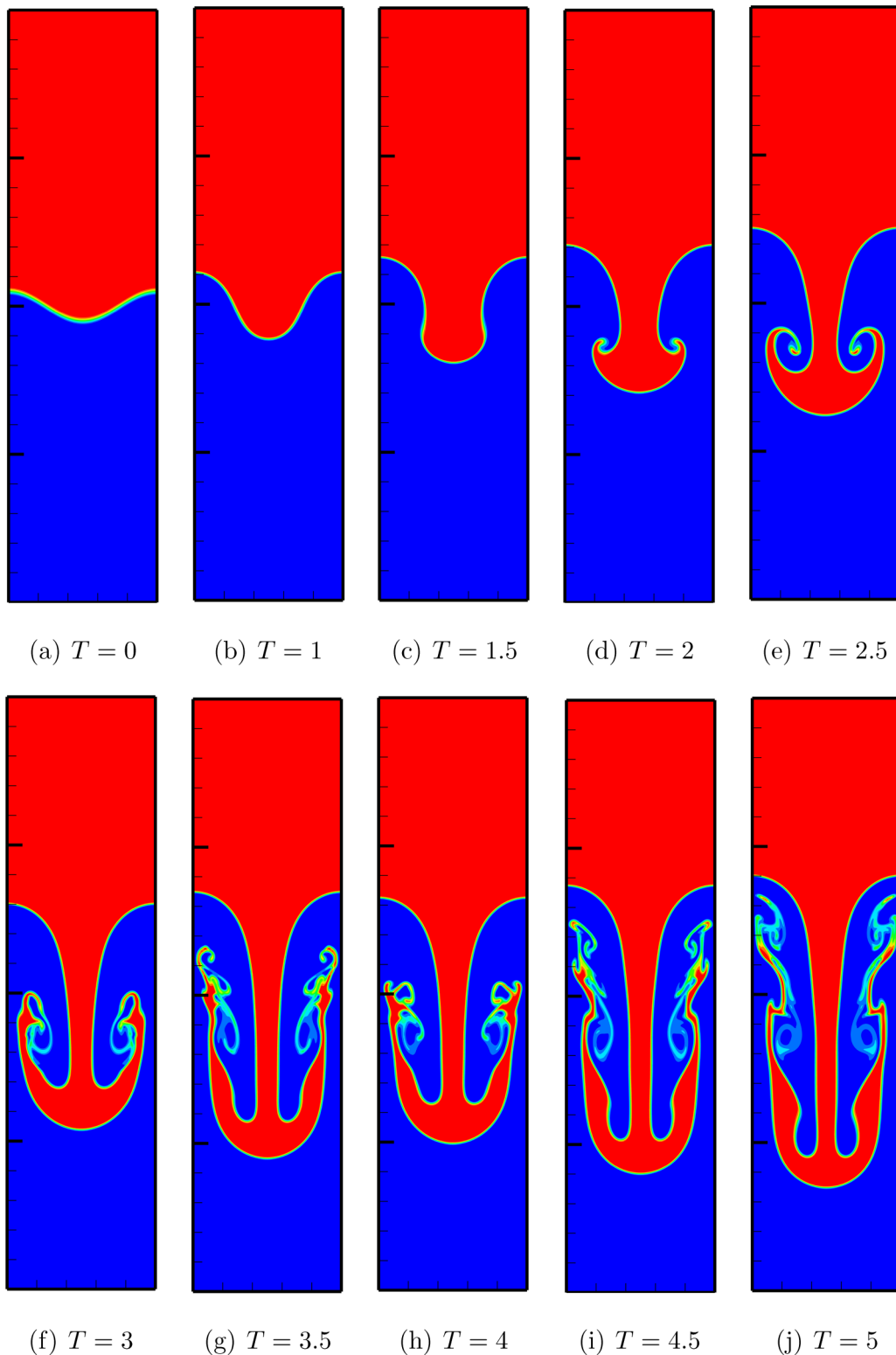


FIG. 18. Evolution of the fluid interface for the 2D Rayleigh-Taylor instability problem at $Re = 2048$.

zero gradients for all variables are applied. Due to symmetry, only one-eighth of the whole flow domain needs to be considered, and a uniform mesh of size $300 \times 150 \times 150$ is adopted. The problem is characterized by two nondimensional parameters, the Reynolds number Re and the Weber number We defined as Eq. (65).

Two cases, which correspond to the experimental situations of tetradecane droplet collision in nitrogen environment at 1 atm pressure conducted by Qian and Law [36], are simulated. The liquid-gas density ratio is 666, and the dynamic viscosity ratio is 119 [37]. The initial positions of the two droplets are $(-D, 0)$ and $(D, 0)$. Other parameters are set as

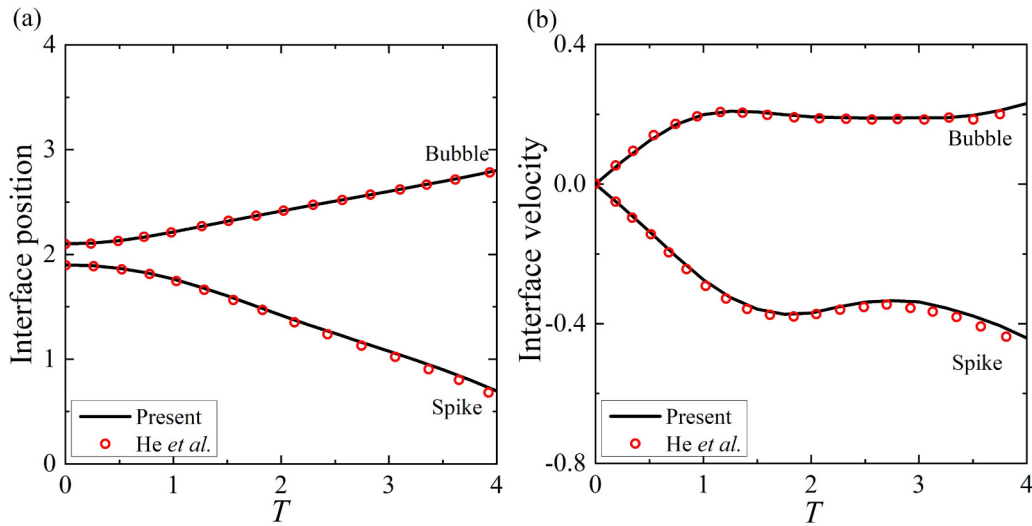


FIG. 19. Positions and velocities of the spike tip and bubble front for the 2D Rayleigh-Taylor instability problem at $Re = 2048$, together with those given by He *et al.* [7].

$U = 0.004$, $D = 100$. According to the experimental parameters, the Weber number and Reynolds number of the two cases are $We = 32.8$, $Re = 210.8$ and $We = 61.4$, $Re = 296.5$, respectively.

Figure 22 shows the transient phase fields on the plane $y = 0$ at different instants. At a low Weber number 32.8, the two droplets merge into a large one first. Then the large droplet stretches and forms a long liquid cylinder with two rounded ends. Owing to a relatively large surface tension, the long liquid cylinder is pulled inwards and remains as one droplet.

This type of collision is classified as the “Coalescence” regime [36]. As to a large Weber number 61.4, the process in which the two droplets merge into a large one and form a long liquid cylinder with two rounded ends can be observed as well. Due to a relatively small surface tension that cannot pull the two rounded ends back, the long liquid cylinder breaks up into three droplets. This type of collision is classified as the “Near head-on separation” regime [36]. All these characteristics are consistent with the corresponding experimental results [36]. Also, the transient phase fields given by RMLBFS match well

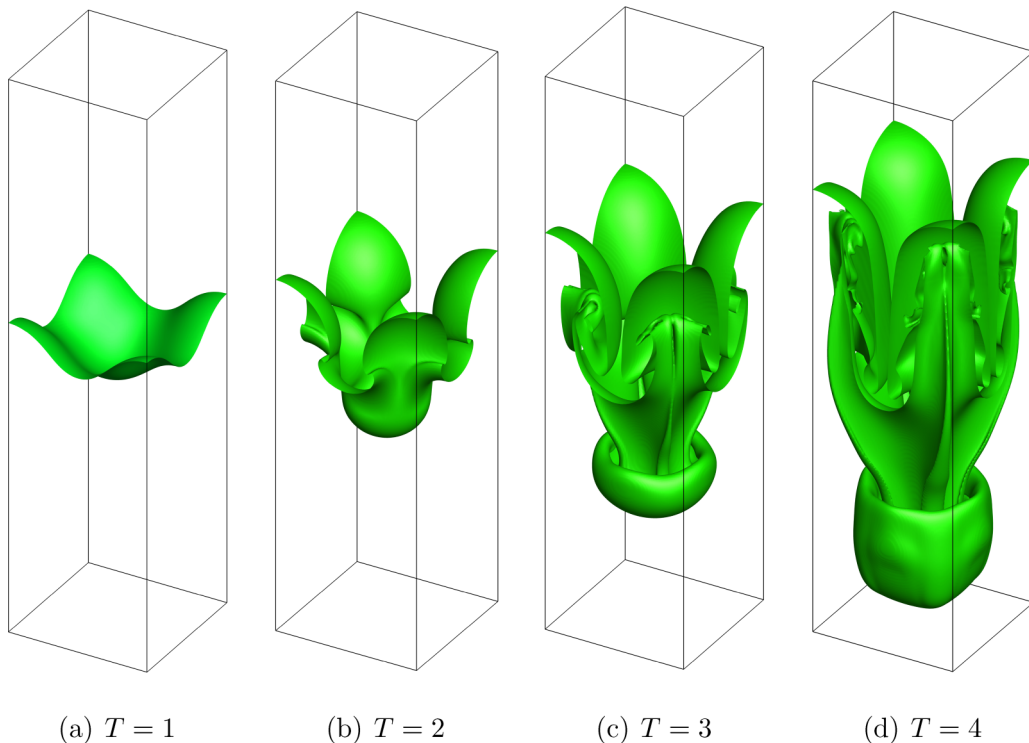


FIG. 20. Interface morphology for the 3D Rayleigh-Taylor instability at $At = 0.5$, $Re = 1024$.

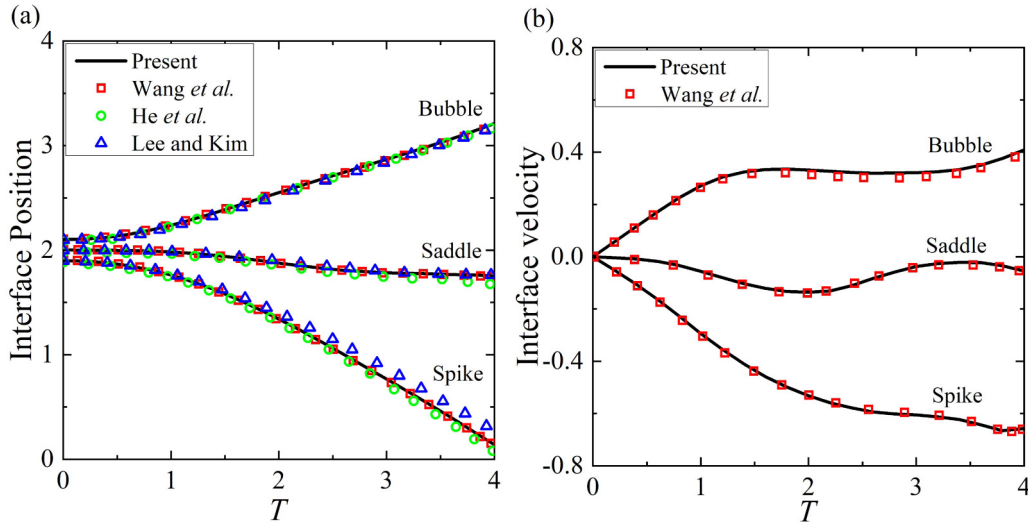
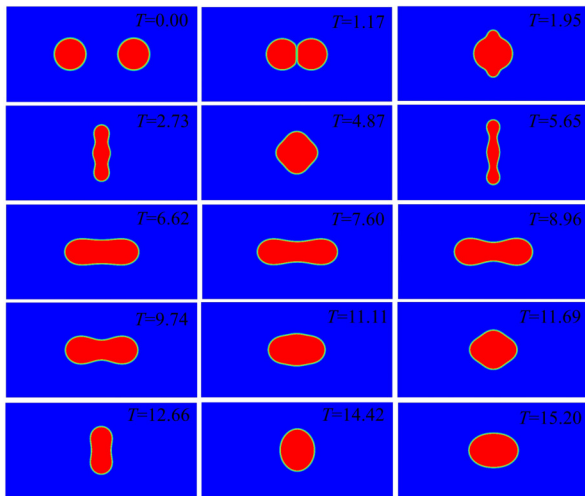
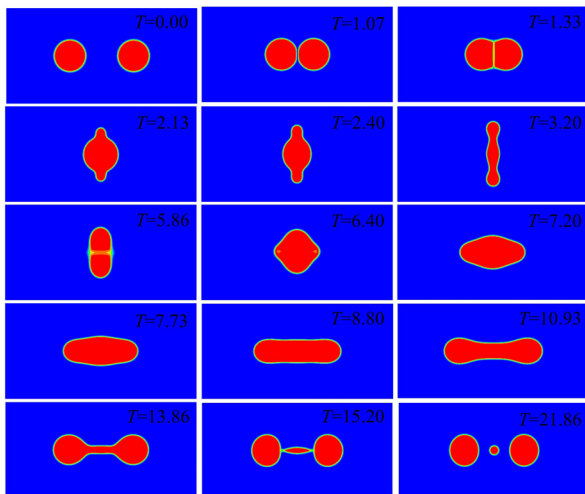


FIG. 21. Positions and velocities of the bubble front, spike tip, and saddle point for 3D Rayleigh-Taylor instability at $At = 0.5$, $Re = 1024$, together with the reference results of He *et al.* [34], Wang *et al.* [21], and Lee and Kim [35].



(a) $We=32.8$, $Re=210.8$



(b) $We=61.4$, $Re=296.5$

FIG. 22. The transient phase fields on the plane $y = 0$ for 3D head-on collisions of binary micro-droplets.

with those simulated by the axisymmetric multiphase lattice Boltzmann method [37].

VI. CONCLUSION

MLBFS is a finite volume solver derived from the lattice Boltzmann model to simulate multiphase flows. It overcomes the limitation of uniform mesh in the lattice Boltzmann method and has been proven to have good numerical stability for multiphase flows with large density ratios. The computational procedures and recovered macroscopic equations indicate that MLBFS is a macroscopic weakly compressible model. In general, weakly compressible models need additional treatments to stabilize computation. As a weakly compressible model, the reasons for the good numerical stability of MLBFS have not been well established. The present work aims to reveal the relation between MLBFS and the macroscopic weakly compressible multiphase model and explain the reason for the good numerical stability of MLBFS from the macroscopic perspective.

In the present paper, MES-MLBFS with actual dissipation terms are derived first by approximating its actual computational process. By solving MES-MLBFS with the finite volume scheme, RMLBFS is constructed. Through detailed numerical investigations, it is found that by combining the predictor step, the corrector step of MLBFS introduces some numerical dissipation terms including pressure diffusion term and bulk viscosity term. These numerical dissipation terms are proven to be essential to stabilize computation. By retaining these numerical dissipation terms, RMLBFS can also achieve good numerical stability at high density ratios and Reynolds numbers. The results indicate that these numerical dissipation terms are the reason for the good numerical stability of MLBFS.

Furthermore, RMLBFS is validated by several benchmark problems. Numerical results show that the same as MLBFS, RMLBFS performs well for both transient and steady multiphase flows even at high density ratios and Reynolds numbers. It further proves the conclusion mentioned above.

ACKNOWLEDGMENTS

J.L. acknowledges the support by the Alexander von Humboldt Foundation, Germany. P.Y. would like to thank

the financial support from the National Natural Science Foundation of China (NSFC, Grant Nos. 91852205) and Department of Education of Guangdong Province (Grant No. 2020KZDZX1185).

-
- [1] G. R. McNamara and G. Zanetti, *Phys. Rev. Lett.* **61**, 2332 (1988).
- [2] A. K. Gunstensen, D. H. Rothman, S. Zaleski, and G. Zanetti, *Phys. Rev. A* **43**, 4320 (1991).
- [3] X. Shan and H. Chen, *Phys. Rev. E* **47**, 1815 (1993).
- [4] X. Shan and H. Chen, *Phys. Rev. E* **49**, 2941 (1994).
- [5] R. Huang, H. Wu, and N. A. Adams, *Phys. Rev. E* **99**, 023303 (2019).
- [6] M. R. Swift, W. R. Osborn, and J. M. Yeomans, *Phys. Rev. Lett.* **75**, 830 (1995).
- [7] X. He, S. Chen, and R. Zhang, *J. Comput. Phys.* **152**, 642 (1999).
- [8] H. Huang, M. Sukop, and X. Lu, *Multiphase Lattice Boltzmann Methods: Theory and Application* (John Wiley & Sons, Inc., 2015).
- [9] S. Leclaire, M. Reggio, and J.-Y. Trépanier, *Comput. Fluids* **48**, 98 (2011).
- [10] Y. Ba, H. Liu, Q. Li, Q. Kang, and J. Sun, *Phys. Rev. E* **94**, 023310 (2016).
- [11] Q. Li, K. H. Luo, and X. J. Li, *Phys. Rev. E* **87**, 053301 (2013).
- [12] H. Zheng, C. Shu, and Y.-T. Chew, *J. Comput. Phys.* **218**, 353 (2006).
- [13] T. Lee and C.-L. Lin, *J. Comput. Phys.* **206**, 16 (2005).
- [14] A. Fakhari, T. Mitchell, C. Leonardi, and D. Bolster, *Phys. Rev. E* **96**, 053301 (2017).
- [15] X. He, L.-S. Luo, and M. Dembo, *J. Comput. Phys.* **129**, 357 (1996).
- [16] C. Shu, Y. T. Chew, and X. D. Niu, *Phys. Rev. E* **64**, 045701(R) (2001).
- [17] J. Tölke, M. Krafczyk, and E. Rank, *J. Stat. Phys.* **107**, 573 (2002).
- [18] D. J. Mavriplis, *Comput. Fluids* **35**, 793 (2006).
- [19] Y. Wang, C. Shu, H. Huang, and C. Teo, *J. Comput. Phys.* **280**, 404 (2015).
- [20] Y. Shi, G. Tang, and Y. Wang, *J. Comput. Phys.* **314**, 228 (2016).
- [21] Y. Wang, C. Shu, and L. Yang, *J. Comput. Phys.* **302**, 41 (2015).
- [22] X.-D. Liu, S. Osher, and T. Chan, *J. Comput. Phys.* **115**, 200 (1994).
- [23] Y. Li, X.-D. Niu, Y. Wang, A. Khan, and Q.-Z. Li, *Int. J. Multiphase Flow* **116**, 100 (2019).
- [24] L. Yang, C. Shu, Z. Chen, Y. Wang, and G. Hou, *Int. J. Numer. Methods Fluids* **93**, 1895 (2021).
- [25] L. Yang, C. Shu, Z. Chen, G. Hou, and Y. Wang, *Phys. Fluids* **33**, 033306 (2021).
- [26] T. Ohwada and P. Asinari, *J. Comput. Phys.* **229**, 1698 (2010).
- [27] T. Ohwada, P. Asinari, and D. Yabusaki, *Comput. Math. Appl.* **61**, 3461 (2011).
- [28] J. Lu, H. Lei, C. Dai, L. Yang, and C. Shu, *J. Comput. Phys.* **453**, 110923 (2022).
- [29] J. Lu, C. Dai, and P. Yu, *Phys. Fluids* **33**, 107120 (2021).
- [30] J. R. Clausen, *Phys. Rev. E* **87**, 013309 (2013).
- [31] A. Kajzer and J. Pozorski, *Flow, Turbul. Combust.* **105**, 299 (2020).
- [32] P. J. Dellar, *Phys. Rev. E* **64**, 031203 (2001).
- [33] C. Josserand and S. Zaleski, *Phys. Fluids* **15**, 1650 (2003).
- [34] X. He, R. Zhang, S. Chen, and G. D. Doolen, *Phys. Fluids* **11**, 1143 (1999).
- [35] H. G. Lee and J. Kim, *Comput. Math. Appl.* **66**, 1466 (2013).
- [36] J. Qian and C. K. Law, *J. Fluid Mech.* **331**, 59 (1997).
- [37] K. Sun, M. Jia, and T. Wang, *Int. J. Heat Mass Transf.* **58**, 260 (2013).